arXiv:astro-ph/0509812 v1   27 Sep 2005

A SPECTROSCOPIC STUDY OF THE ANCIENT MILKY WAY: F- AND G-TYPE STARS IN THE THIRD DATA RELEASE OF THE SLOAN DIGITAL SKY SURVEY

Carlos Allende Prieto
McDonald Observatory and Department of Astronomy, University of Texas, Austin, TX 78712

Timothy C. Beers
Department of Physics & Astronomy and JINA: Joint Institute for Nuclear Astrophysics,
Michigan State University, E. Lansing, MI 48824

Ronald Wilhelm
Department of Physics, Texas Tech University, Lubbock, TX 79409

Heidi Jo Newberg
Rensselaer Polytechnical Institute, Troy, NY 12180

Constance M. Rockosi
UCO/Lick Observatory, 1156 High St., Santa Cruz, CA 95064

Brian Yanny
Fermi National Accelerator Laboratory, P.O. Box 500, Batavia, IL 60510

AND

Young Sun Lee
Department of Physics & Astronomy and JINA: Joint Institute for Nuclear Astrophysics,
Michigan State University, E. Lansing, MI 48824
Accepted for publication in the ApJ

ABSTRACT

We perform an analysis of spectra and photometry for 22,770 stars included in the third data release (DR3) of the Sloan Digital Sky Survey (SDSS). We measure radial velocities and, based on a model-atmosphere analysis, derive estimates of the atmospheric parameters (effective temperature, surface gravity, and [Fe/H]) for each star. Stellar evolution models are then used to estimate distances. We thoroughly check our analysis procedures using three recently published spectroscopic libraries of nearby stars, and compare our results with those obtained from alternative approaches. The SDSS sample covers a range in stellar brightness of $14 < V < 22$, primarily at intermediate galactic latitudes, and comprises large numbers of F- and G-type stars from the thick-disk and halo populations (up to 100 kpc from the galactic plane), therefore including some of the oldest stars in the Milky Way.

In agreement with previous results from the literature, we find that halo stars exhibit a broad range of iron abundances, with a peak at [Fe/H] $\simeq -1.4$. This population exhibits essentially no galactic rotation. Thick-disk G-dwarf stars at distances from the galactic plane in the range $1 < |z| < 3$ kpc show a much more compact metallicity distribution, with a maximum at [Fe/H] $\simeq -0.7$, and a median galactic rotation velocity at that metallicity of 157 ± 4 km s^{-1} (a lag relative to the thin disk of 63 km s^{-1}). SDSS DR3 includes spectra of many F-type dwarfs and subgiants between 1 and 3 kpc from the plane with galactic rotation velocities consistent with halo membership. A comparison of color indices and metal abundances with isochrones indicates that no significant star formation has taken place in the halo in the last ~ 11 Gyr, but there are thick-disk stars which are at least 2 Gyr younger. We find the metallicities of thick-disk stars to be nearly independent of galactocentric distance between 5 and 14 kpc from the galactic center, in contrast with the marked gradients found in the literature for the thin disk. No vertical metallicity gradient is apparent for the thick disk, but we detect a gradient in its rotational velocity of -16 ± 4 km s^{-1} kpc^{-1} between 1 and 3 kpc from the plane. We estimate that among the stars in our sample there are over 2000 with an iron abundance [Fe/H] < -2, and over 150 stars with an iron abundance [Fe/H] < -3.

Subject headings: stars: fundamental parameters, abundances — Galaxy: stellar content — Galaxy: structure — Stars: Population II — Stars: Galactic Halo — Stars: Thick Disk

Electronic address: callende@astro.as.utexas.edu

1. INTRODUCTION

Our present view of the structure of the Milky Way is mainly built upon star counts. The most recent applications of this classical approach converge to two-component disk models with scale heights of $Z^h_{\rm thin} \sim 0.2 - 0.3$ kpc and $Z^h_{\rm thick} \sim 0.6 - 1.0$ kpc, and a normalization factor $\rho_{\rm thick}/\rho_{\rm thin} \sim 0.02 - 0.13$. Two more spheroidal components are needed to account for the observed numbers of stars, a central bulge and a halo. The density distribution of the stellar halo is still poorly constrained, but it extends to distances in excess of 100 kpc from the galactic plane, and its density in the plane is likely a fraction of a percent of the thin disk density (Norris 1999; Chen et al. 2001; Siegel et al. 2002; Larsen & Humphreys 2003; Robin et al. 2003; Cabrera-Lavers, Garzón & Hammersley 2005).

The derivation of stellar densities from star counts involves several assumptions. For example, only very rough information on chemical composition and luminosity is available from broad-band photometric observations alone, forcing practitioners to adopt pre-determined relationships, and to rely on the hypothesis that dwarfs outnumber evolved stars in any given field. Spectroscopic surveys of galactic stars, despite being of necessity biased in order to sample low-density populations (such as the galactic halo in the solar neighborhood), are extremely valuable to complement star count analyses and unravel co-existing stellar populations. Kinematics and chemical abundances expand our view of the Galaxy from a snapshot provided by star counts to a more dynamical perspective, allowing the study of not just the present structure of the Milky Way, but to peer into its formation and evolution (see, e.g., Chiba & Beers 2000, 2001; Freeman & Bland-Hawthorn 2002; Nordström et al. 2004).

Extensive spectroscopic surveys with high spectral resolution have so far been primarily restricted to the solar neighborhood. Single-object spectrographs delivering medium-resolution spectra have been the workhorse for studies of large numbers of more distant stars (e.g., Beers, Preston, & Shectman 1992; Beers 1999; Wilhelm et al. 1999b; Brown et al. 2003; Christlieb 2003), but recently, highly-multiplexed spectrographs have made possible an increase of the data acquisition rate by several orders of magnitude. The near future is even more exciting, with the advent of planned new instruments able to gather spectra for thousands of targets simultaneously, over large fields, at high spectral resolution, and without gaps in solid-angle (e.g., Hill & MacQueen 2002; Moore, Gillingham, & Saunders 2002).

The now-completed Sloan Digital Sky Survey (York et al. 2000; SDSS) has imaged about one fourth of the sky with five broad-band filters and obtained follow-up intermediate dispersion ($R \equiv \lambda/{\rm FWHM} \sim 2000$) spectroscopy of numerous targets. In its spectroscopic mode, up to 640 fibers can be simultaneously positioned on the focal plane of the SDSS 2.5m telescope to feed two identical spectrographs, both providing continuous coverage in the range 381-910 nm (Newman et al. 2004).

The criteria for selecting SDSS spectroscopic targets are rather complex (see Strauss et al. 2002 and references therein). Galaxies and quasar candidates take about 90% of the fibers; the remaining fibers are used to observe the sky background and galactic stars. The stars are either selected for being of special interest (e.g., white dwarfs, blue horizontal-branch stars, carbon stars, late-type M-dwarfs, brown dwarf candidates, etc.), or because they lie within a narrow color range intended for refinement of reddening determinations or flux calibration. In addition, a fraction of the SDSS quasar candidates turned out to be stars (Stoughton et al. 2002). With exposure times of the order of 45 minutes, the targeted stars have V magnitudes in the range 14–22, signal-to-noise ratios (S/N) between 4 and 60, and lie at distances of up to a few hundred kiloparsecs from the galactic plane. More than 10^5 stellar spectra will be released to the public by the end of 2006. Nearly 50,000 stellar spectra were made publicly available in the second data release (Abazajian et al. 2004; hereafter DR2), and an additional $\sim$ 20,000 stellar spectra followed as part of DR3 (Abazajian et al. 2005). DR4 became public on July 2005 (Adelman-McCarthy et al. 2005), expanding the public database with over 12,000 new stellar spectra.

Among the stellar targets in the SDSS database, low-mass stars are of particular interest because they have long lives and thus can be used to trace the chemical evolution of the Galaxy. In principle, the numbers of low-mass stars at different metallicities reflects the history of star formation and galaxy assembly. Accurate analysis of relative chemical abundances is now routinely possible for F- and G-type stars within the framework of classical one-dimensional model atmospheres (but see, e.g., Asplund 2005 for caveats). Most of the stars in DR3 belong to these categories.

In this paper we begin a detailed exploration of this extensive database. We have used SDSS photometry and spectra to derive stellar atmospheric parameters, radial velocities, and distance estimates for a significant fraction of the stars included in DR3. The dataset and the analysis procedure are described in §2. In §3, we thoroughly test our derived parameters by comparing with three spectroscopic libraries of nearby stars with reliable physical parameters. In §4 we examine the distributions of stars in DR3, their iron abundances, and their kinematics at different distances from the galactic plane and from the galactic center. In §5, we conclude with a brief summary and comment on research to follow. Readers who wish to skip the technical details might wish to resume in §4.

2. DESCRIPTION OF THE DATASET AND OUR MODEL-ATMOSPHERE ANALYSIS

DR3 contains 528,640 spectra from 574 plugplates, covering 2527 deg^2 on the sky. The SDSS pipeline classified 71,397 of the DR3 spectra as STARs. These data were pre-processed and analyzed as described below.

2.1. *Pre-processing of DR3 stellar spectra and gr photometry*

SDSS $ugriz$ photometry is available for all the objects with spectra. The signal-to-noise ratio per pixel for the SDSS spectra is larger than 4 at $g = 20.2$, and the wavelength calibration is accurate to better than 5 km s^{-1}. A number of improvements have been made to the SDSS spectroscopic pipeline for DR2/DR3, in particular to the spectrophotometric calibration and to the determination of radial velocities, as compared to data released in DR1 and the early data release (EDR). For each plugplate,

16 fibers are allocated to F-type stars that serve as reddening or spectrophotometric calibrators (in equal proportions). The relative flux calibration is obtained by assigning a spectral type to each calibration star, and using synthetic spectra based on Kurucz's model atmospheres to remove the instrumental response. Absolute fluxes are derived by forcing the r-band magnitudes computed from the corrected calibration spectra to match the r magnitudes from the calibrators measured by the photometric pipeline. For more details we refer the reader to Stoughton et al. (2002) and Abazajian et al. (2004, 2005).

Heliocentric velocity corrections have already been calculated and applied to archival SDSS spectra, which are distributed on a logarithmic vacuum wavelength scale. Doppler shifts in the stellar spectra are measured by cross-correlation with observed templates in the SDSS pipeline. As part of our data pre-processing, we change the wavelength scale to standard air (Edlén 1966), and re-sample the spectra linearly. Assuming that the SDSS spectrographs deliver $\mathsf{R} \simeq 2000$, independent of wavelength, we smooth the spectra to a resolving power $\mathsf{R} \simeq 1000$ by convolution with a Gaussian profile equivalent to $\mathsf{R}_\mathrm{G} = 1155$. This step is taken following tests with EDR spectra, which indicated that for our purposes it is advantageous to trade resolution for S/N. The uncertainties provided as part of the SDSS are also corrected for the change in resolution.

We first determine the velocity shifts of several strong features (Hα, Hβ, Hγ, Hδ, and CaII K) to obtain an independent measurement of the stellar radial velocities and their uncertainties. The spectra in which we could not identify Balmer lines were not considered for further analysis, as they are either very hot, very noisy, exhibit emission features, or are too cool, and thus unsuitable for the analysis techniques described below. The reference wavelengths were derived from the solar spectrum observed at much higher resolving power and smoothed to the appropriate resolution. The spectra are then shifted in velocity to the rest frame and re-sampled with three data points per resolution element.

We identified Balmer lines and derived radial velocities for 44,175 DR3 stars. Fig. 1 compares our derived velocities with those provided by the SDSS pipeline (zc, as they are coded as a redshift in the FITS headers) for 30,589 objects with colors in the range $0.0 \lesssim (g-r) \lesssim 0.7$ mag. This corresponds, roughly, to stars with $5000 < T_\mathrm{eff} < 8000$ K. On average, our radial velocities are smaller by roughly 5 km s^{-1}. Removing the zero-point offset, and excluding far outliers, the two scales agree with a 1σ scatter of 12 km s^{-1}, although the residuals are not Gaussian, as illustrated in Fig. 1. Most of the stars are contained within the range $-500 < V_r < 500$ km s^{-1}, but there are about 20 objects with velocities between $500 < V_r < 1000$ km s^{-1} for which there is good agreement between the values from the pipeline and our measurements. Such velocities exceed the escape velocity from the Galaxy, and therefore a few of these objects may belong to the same class as the hyper-velocity star recently reported by Brown et al. (2005). The majority appear to be galaxies in the Virgo cluster, mistaken for stars by the SDSS classifiers.

Most of the spectral information that can be used to constrain the atmospheric parameters resides in the blue
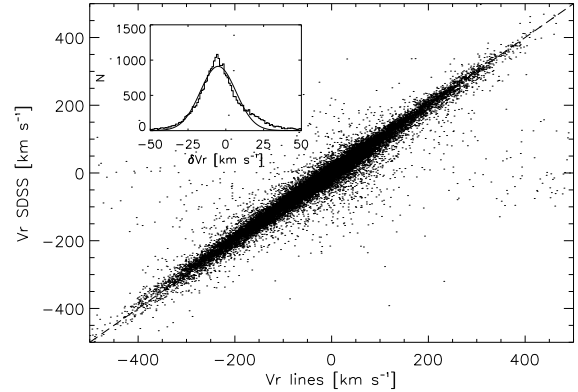

FIG. 1.— Radial velocities derived from the Doppler shift of strong lines and from the SDSS pipeline. A small systematic zero-point offset is present (see text). The dashed line has a slope of one. The inset shows an histogram of the velocity differences and a Gaussian fit.

region, but the S/N peaks in the red for late-type stars. As a compromise, we trimmed the spectra to the region 440-550 nm, increasing the analysis speed by a factor of about five as compared to an analysis of the full spectral range. The spectra are normalized by iteratively fitting a sixth-order polynomial to the pseudo-continuum, clipping off points that lie farther than 1σ below, or 4σ above the fitting curve. As the absolute flux calibration is tied to the photometric scale of the imaging survey, and the relative spectrophotometry is based on fluxes calculated in a similar way as those we match to the observations in our analysis, little information is lost by applying this correction. In addition, the impact of reddening on the spectra is essentially removed.

In addition to the spectra, we also use SDSS gr photometry to constrain the stellar parameters. Restricting the photometry to the $g-r$ color index makes it possible to perform a fair comparison with the libraries of nearby stars described below, which in most cases only include BV photometry. The reddening in $B-V$ was interpolated from the maps of Schlegel, Finkbeiner & Davis (1998), with the following transformations for the SDSS g and r passbands

$$\begin{aligned} A_g &= 3.793 \; E(B-V) \\ A_r &= 2.751 \; E(B-V). \end{aligned} \tag{1}$$

Given that the location of the vast majority of our targets are at distances larger than 0.5 kpc, and the relatively high galactic latitude of the fields, it seems appropriate to apply the full extinction from the maps.

The pre-processing of DR3 spectra described above can be summarized as follows: we smooth, normalize, velocity correct, re-sample, and truncate the spectra to the spectral region 440–550 nm. Point Spread Function gr photometry is also included in the analysis, after correcting for interstellar extinction. Throughout the paper, we refer exclusively to photometry corrected for reddening.

2.2. Analysis

Our analysis combines spectra and photometric indices from SDSS. We will refer to the data vector as $\mathbf{T} \equiv \{(g-r), S_1, S_2, ..., S_m\}$, where the S_i are the continuum-
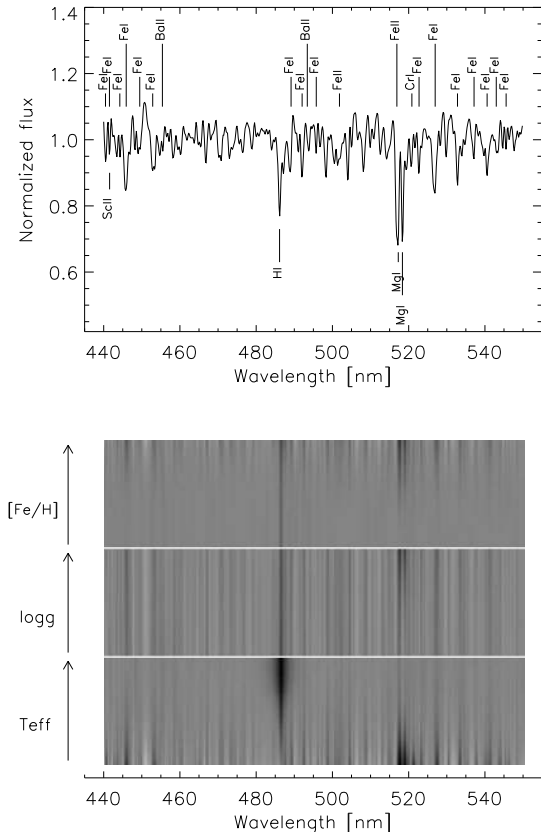
FIG. 2.— *Upper panel* Computed spectrum for a solar-like star; the strongest features due to single transitions are identified. *Lower panel* Variation of the continuum-corrected flux as a function of each of the three atmospheric parameters considered here, with the others fixed at near-solar values.

corrected spectral fluxes, and $m = 667$ for our choice of resolving power and sampling. We model **T** with plane-parallel line-blanketed model atmospheres in local thermodynamical equilibrium (LTE) as a function of the stellar parameters $T_{\rm eff}$, $\log g$, and $[{\rm Fe/H}]$[1]. The model atmospheres are extracted from the Kurucz (1993) grid, which was calculated adopting a mixing-length $l/H_p = 1.25$, and a micro-turbulence of 2 km s^{-1}. A parallel grid of low-resolution (R $\sim$ 300) spectra, computed with detailed line and continuous metal-opacities, has been provided by Kurucz (1993). Synthetic photometric indices are derived from these spectra and the SDSS filter responses (Strauss & Gunn 2001[2]). These indices differ from those presented by Lenz et al. (1998), as the detailed filter responses for the 2.5m telescope were not available at that time. The atmospheric structures are used to produce a second grid of LTE synthetic spectra with a resolving power (R = 1000) and spectral coverage (440–550 nm) matching the pre-processed SDSS spectra. To produce this second grid, we employ the code `synspec` (Hubeny & Lanz 2000), and very simple continuous opacities: H, H$^-$, H Rayleigh and electron scatter-

ing (as described by Hubeny 1988). Atomic line opacity is considered with 37,566 transitions, neglecting molecular opacity, treating Balmer line profiles as in Hubeny, Hummer & Lanz (1994).

The grids of calculated spectra considered here span the ranges [4500,9250] K in $T_{\rm eff}$, [1.5,5.0] in $\log g$, and [−4.83,+0.67] in [Fe/H]. The upper panel of Fig. 2 shows a calculated spectrum for a solar-like star after correcting the continuum shape. This correction is applied to the absolute fluxes in exactly the same manner as to the observed (flux-calibrated) spectra (see §2.1) to ensure consistency. The strongest features due to single transitions have been identified in the figure. Most of the lines are due to iron, and many of the observed features result from multiple overlapping transitions. The lower panel shows three images created by stacking the continuum-corrected spectra (with a grey-scale indicating the flux level) as a function of each of the three atmospheric parameters considered, with the other two fixed at solar values. It is immediately apparent that variations in surface gravity produce the most subtle changes in the spectrum, and that the presence of the Mg I b triplet is key to our ability of constraining this parameter from the observations. The wings of the Mg I b lines are collisionally enhanced, and dominate the gravity-driven changes on the strength of the lines (e.g., Fuhrmann et al. 1997).

Model spectra and photometry for sets of parameters off the grid nodes are derived by interpolation (Allende Prieto 2004). The high speed required to classify such a large sample is achieved at the expense of using a fairly coarse mesh, with $12 \times 15 \times 19$ nodes in $T_{\rm eff} - \log g - [{\rm Fe/H}]$, selected to match the nodes of the available grid of model atmospheres, avoiding interpolations in the atmospheric structures.

We adopted reference solar abundances as in Asplund, Grevesse & Sauval (2004). These solar abundances include the recently revised values of the photospheric C, O, and Fe abundances, which are roughly 0.2 dex lower than those used by Kurucz (1993). Thus, we corrected for this amount in the selection of the atmospheric structures and low-resolution fluxes from Kurucz's grid. Some chemical elements have abundance ratios to iron that are non-solar in metal-poor stars; this is largely ignored in our modeling. However, we do take into account enhancements to the abundances of the α elements Mg, Si, Ca, and Ti in metal-poor stars when calculating synthetic spectra. Following Beers et al. (1999), we adopt

$$[\alpha/{\rm Fe}] = \begin{cases} 0 & \text{if } [{\rm Fe/H}] \geq 0 \\ -0.267\,[{\rm Fe/H}] & \text{if } -1.5 \leq [{\rm Fe/H}] < 0 \\ +0.4 & \text{if } [{\rm Fe/H}] < -1.5. \end{cases} \quad (2)$$

The above recipe will work well for thin-disk stars and low-metallicity halo stars, but it will underestimate the $[\alpha/{\rm Fe}]$ ratios in halo and thick-disk stars with [Fe/H] > -1. The systematic errors will affect thick-disk stars the most, given that they concentrate in that metallicity regime. The [Mg/Fe] abundance ratio for thick-disk members remains as high as ~ 0.3 dex up to [Fe/H] $\simeq -0.4$ (Fuhrmann 1998; Prochaska et al. 2000; Bensby, Feltzing & Lundström 2003; Reddy et al. 2003; Brewer

---

[1] Following standard use, $T_{\rm eff}$ is the effective temperature, g is the surface gravity (given in cm s^{-2} throughout the text), and $[{\rm Fe/H}] = \log_{10}(N({\rm Fe})/N({\rm H})) - \log_{10}(N({\rm Fe})/N({\rm H}))_\odot$, where N represents number density.

[2] http: //archive.stsci.edu/sdss/documents/response.dat

& Carney 2005; Reddy, Lambert & Allende Prieto 2005), and Eq. 2 would therefore underestimate this ratio by ~ 0.2 dex for such stars. Because the strength of the wings of the Mg I b lines is proportional to both the Mg abundance and the density of the collisional perturbers (mostly H atoms), underestimating the former would be compensated by a similar error of opposite sign in the gas pressure, resulting in surface gravity estimates which are too high by about 0.2 dex. Although such biases are not negligible, they are smaller than the typical uncertainties in the surface gravities that we derive from the SDSS data.

We search for the model parameters that minimize the distance between the model flux vector $\mathbf{T}$ ($T_{\rm eff}$, $\log g$, [Fe/H]), and the observation vector $\mathbf{O}$ in a χ^2 fashion

$$\mu = \sum_{i=1}^{m+1} \frac{W_i}{\sigma_i^2} (O_i - T_i)^2 \qquad (3)$$

where the weights W_i were set equal for all the data points in a spectrum, about two orders of magnitude larger for the photometric index $(g-r)$, and normalized $\sum W_i = m+1$.

The search is accomplished using the Nelder-Mead simplex method (Nelder & Mead 1965). This optimization algorithm, combined with interpolation, performs well in terms of accuracy and speed, processing several stars per second on a modern workstation. Error bars for the spectral fluxes are available as part of the SDSS data, and we have accounted for the reduction of resolution in our pre-processing (see §2.1). The weighted S/N ratio is derived

$$S/N = \sqrt{\frac{1}{m+1} \sum_{i=1}^{m+1} \frac{W_i}{\sigma_i^2}}, \qquad (4)$$

and $\sigma_1 \equiv \sigma_{(g-r)}$ is estimated from the signal-to-noise ratio of the spectrum

$$(S/N)_s = \sqrt{\frac{1}{m} \sum_{i=2}^{m+1} \frac{1}{\sigma_i^2}}, \qquad (5)$$

and an empirical relationship for SDSS data

$$\sigma_{(g-r)} = \begin{cases} 0.131 & \text{if } (S/N)_s < 11.500024 \\ 0.02 & \text{if } (S/N)_s > 57.5 \\ 0.02 - \frac{1}{130.4} \ln\left(\frac{(S/N)_s - 11.5}{46}\right) & \text{else.} \end{cases} \qquad (6)$$

The S/N of the spectra smoothed to $R \simeq 1000$ is approximately 2.3 times higher than that of the original data. Fig. 3 illustrates the weighted S/N of our processed spectra as a function of $(S/N)_s$. The vast majority of the stars have $20 < S/N < 100$; stars with $S/N < 30$ are not considered in this study.

The effective temperature, $T_{\rm eff}$, is fairly well-constrained for most stars. The metallicity, [Fe/H], is tightly confined for the metal-rich and cooler stars in our sample, but degrades for warmer stars, and especially so for the most metal-poor cases. The surface gravity, $\log g$, is the most poorly constrained parameter. Fig. 4 shows two examples of the matching between observed
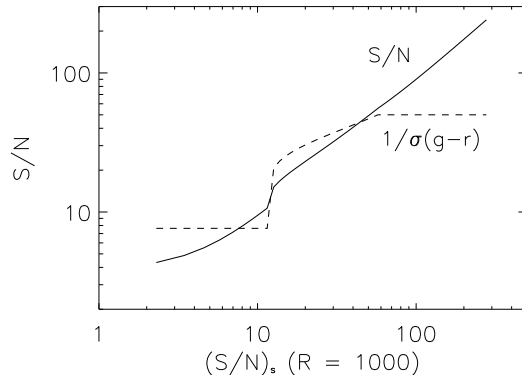

FIG. 3.— The weighted S/N for DR3 stars as used here is defined as the square root of a linear combination of the signal-to-noise of the spectrum $(S/N)s$ and that of the color index $(g-r)$, which is tied to the former by an empirical recipe (Eq. 6).

and model fluxes, as well as the variations of $\log \chi^2$ in planes across the optimal solutions. The observed and calculated photometric indices, $(g-r)$, are shown at an arbitrary wavelength in the upper panels. Other techniques for obtaining estimates of atmospheric parameters have also been explored, and we compare them with our minimum-distance method in Section 3.6.

Fig. 5 shows the final reduced $\chi^2 = \mu/m$ for the sample. Most stars have late-F and early-G spectral types, and few are warmer than about 7000 K. Late-G and early-K stars are fit somewhat worse than warmer spectral types, mostly due to an increased importance of the metal line opacity, which is afflicted by poor and missing atomic data. The two cases illustrated in Fig. 4 have a reduced χ^2 of 1.2 and 0.7, for the more metal-rich and more metal-poor star, respectively.

Once the atmospheric parameters are defined, we make use of stellar evolution calculations by the Padova group (Alongi et al. 1993; Bressan et al. 1993; Bertelli et al. 1994; Fagotto et al. 1994) to find the best estimates for other stellar parameters, such as radius, M_V, mass, etc. With the atmospheric parameters and their uncertainties in hand we define a normalized probability density distribution that is Normal for $T_{\rm eff}$ and $\log g$, and a boxcar function in $\log(Z/Z_\odot)$

$$P \propto \exp\left[-\left(\frac{T_{\rm eff} - T_{\rm eff}^*}{\sqrt{2}\sigma(T_{\rm eff})}\right)^2\right] \qquad (7)$$

$$\times \exp\left[-\left(\frac{\log g - \log g^*}{\sqrt{2}\sigma(\log g)}\right)^2\right] B\left(\log(Z/Z_\odot)\right),$$

which is then used to find the best estimate of a stellar parameter X by integration over the space ($Z/Z_\odot$, Age, and initial mass M) that characterizes the stellar isochrones of Bertelli et al. (1994):

$$\bar{X} = \int \int \int X P(Z/Z_\odot, Age, M) d(Z/Z_\odot) d(Age) dM. \qquad (8)$$

Our method follows that described in the Appendix A of Allende Prieto, Barklem, Lambert, & Cunha (2004a),
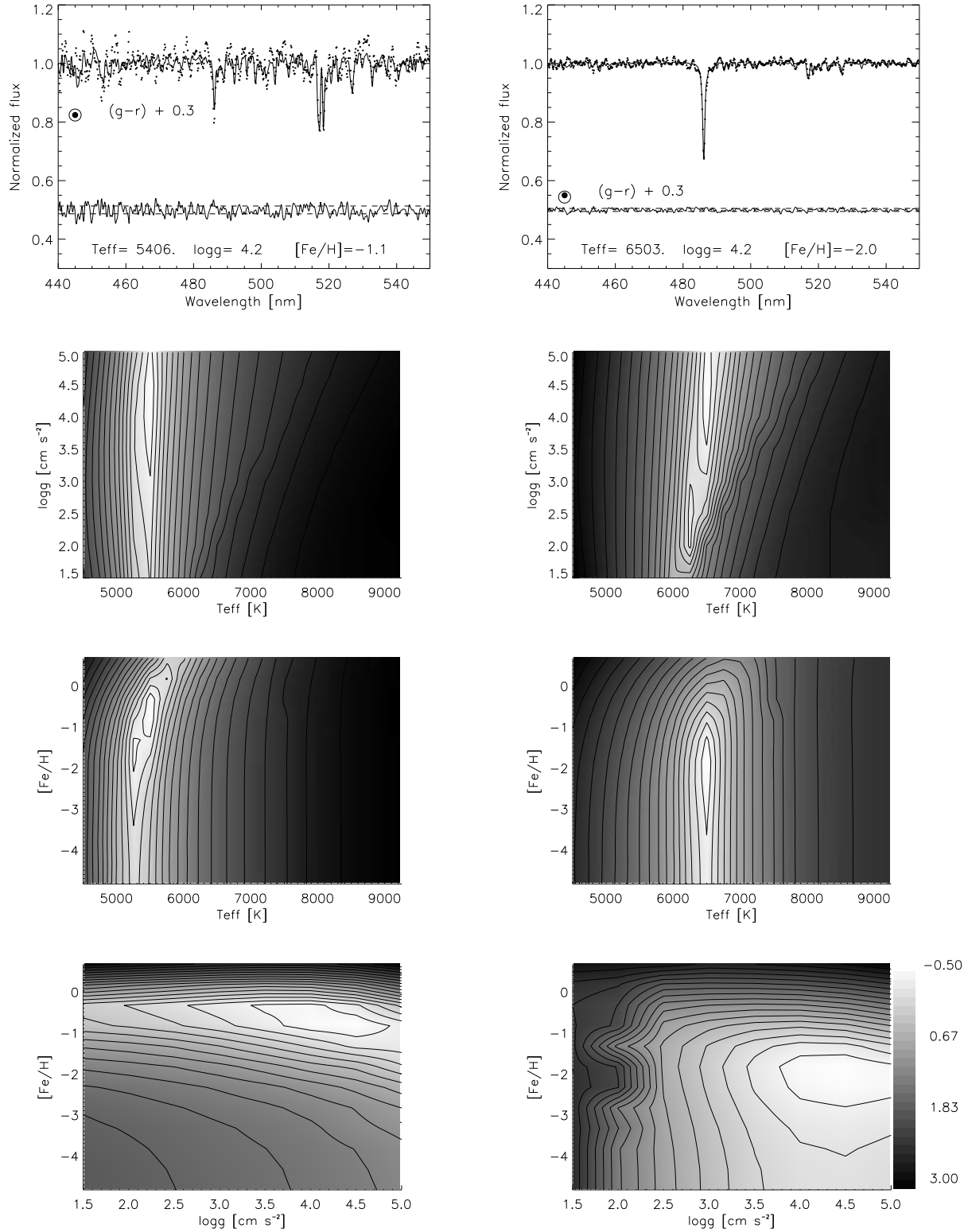
Allende Prieto et al.

FIG. 4.— Two examples of our data analysis. The graphs on the left correspond to the object SDSS J135701+520018.4, a G-type subgiant with a metallicity [Fe/H] ∼ −1 ($T_{\rm eff}$ = 5406 K, $\log g$ = 4.2, [Fe/H] = −1.1); the right-hand-side panels are for SDSS J135526+512938.1, an F-type metal-poor dwarf ($T_{\rm eff}$ = 6503 K, $\log g$ = 4.2, [Fe/H] = −2.0). The top panels compare the observed (filled circles) and the best-fitting spectra (solid line), as well as the observed $g-r$ (large filled circles) with the best-fitting indices (open circles), shown at an arbitrary wavelength. The lower solid lines in each of the top panels indicates the residuals obtained from the best-fitting spectra plus 0.45, while the dashed lines mark the average error of the fluxes. The lower panels show the variations in the logarithm of the reduced $\chi^2 = \log(\mu/m)$ in planes that cross the optimal solutions. Three-sigma errors approximately correspond to deviations of +1 from the minimum in the gray scale.
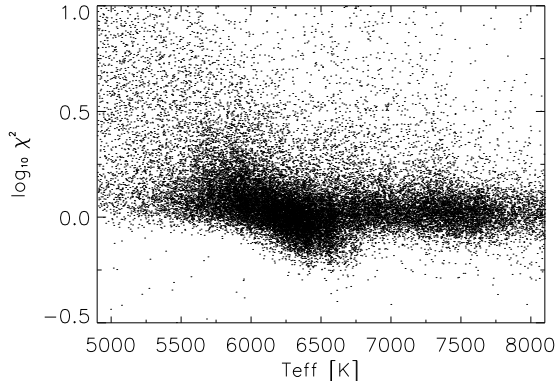
FIG. 5.— Variation of the reduced χ^2 as a function of the effective temperature for the sub-sample of 44,175 DR3 stars with spectra for which we detected Balmer lines.

where more details can be found; in our case we adopted $\sigma(T_{\rm eff}) = 150$ K, and $\sigma(\log g) = 0.3$ dex for all stars. The boxcar is a justified simplification, and we adopted a width of 0.3 dex. The isochrones employed do not consider enhancements in the abundances of the α elements for metal-poor stars. To compensate for this effect we follow Degl'Innocenti, Prada Moroni, & Ricci (2005) and equate

$$Z/Z_\odot = 10^{[{\rm Fe/H}]}(0.659 \times 10^{[\alpha/{\rm Fe}]} + 0.341), \qquad (9)$$

with $[\alpha/{\rm Fe}]$ as given in Eq. 2. The isochrones have metallicities between $0.02 \leq Z/Z_\odot \leq 2.5$. For stars with metallicities $[{\rm Fe/H}] < -2$, we use isochrones with $Z/Z_\odot = 0.02$. We do not expect significant changes in the structure and evolution of low-mass stars between this metallicity levels and zero metallicity, hence this approximation is unlikely to be a source of large systematic errors. Our tests indicate that use of updated isochrones with similar abundance ratios published by the Padova group (e.g., Girardi et al. 2004) would lead to very similar results.

From the magnitudes in the SDSS passbands we estimate the Johnson V magnitudes of the stars using the transformation derived by Zhao & Newberg (private communication; see Eq. 12 below). This transformation, and others which are part of the same work, were derived from a sample of 58 metal-poor and field horizontal branch stars previously identified in the HK survey (Beers et al. 1999) with both UBV and $u^*g^*r^*i^*z^*$ photometry. They should be considered as approximate for our purposes, given that they are not referred to the exact same photometric system as the DR3 magnitudes ($u^*g^*r^*i^*z^*$ vs. $ugriz$). Knowing M_V and the reddening, it is then straightforward to derive distances.

3. REFERENCE CALIBRATIONS AND CONSISTENCY CHECKS

We have selected three libraries of stellar spectra for checking our analysis procedure: the Indo-US library of Coudé feed stellar spectra (Valdes et al. 2004, hereafter `Cflib`), the Elodie library (Prugniel & Soubiran 2001, hereafter ELODIE), and the Spectroscopic Survey of Stars in the Solar Neighborhood (Allende Prieto et al. 2004,

hereafter S^{4}N). These libraries include photometry; in particular, all of them list Johnson B and V magnitudes, which can be used to estimate $(g-r)$, with the transformation derived by Zhao & Newberg:

$$(g - r) = 1.043(B - V) - 0.185. \qquad (10)$$

In addition to spectra and photometry, the chosen libraries provide catalogs of atmospheric stellar parameters that can be considered reliable, based on a consistent analysis of the spectra in the library and/or collated from high-dispersion studies in the literature. Our comparison with the libraries of nearby stars, and our later analysis of stellar spectra in DR3, is restricted to the range $5000 < T_{\rm eff} < 8000$ K. Outside these limits in effective temperature, our results degrade significantly, due to systematic differences in the temperature scale on the warm side, and a degeneracy between metallicity and temperature for the cool stars. Work is underway to improve these limitations for future analysis of SDSS stars.

3.1. `Cflib`

`Cflib` contains 885 stars with a spectral coverage similar to the SDSS spectra, gathered with the 0.9m Coudé feed telescope at Kitt Peak National Observatory [3]. The S/N ratio is relatively high, typically larger than 200, and the spectral resolution is about 1.2 Å, about a factor of two higher than SDSS spectra. We smoothed the spectra with a Gaussian kernel to match our working resolving power R $\simeq 1000$. Fig. 6 compares the atmospheric parameters in the library's catalog, which were compiled from high-resolution studies in the literature, with those we derived (FIT) for 333 stars in the effective temperature range $5000 < T_{\rm eff} < 8000$ K, discarding 54 stars which could not be fit with a reduced $\chi^2 < 20$. Our effective temperatures are in good agreement with the catalog values. By fitting a Gaussian to the residuals (see Fig. 6), we derive a mean offset of 1%, and a 1σ scatter of 3%. Our gravities are consistent with the catalog's, with a scatter of 0.30 dex, and an offset of $+0.02$ dex. Our iron abundances are also on the same scale as those in the `Cflib` catalog, with a scatter of only 0.16 dex.

3.2. ELODIE

This library contains spectra obtained with the ELODIE spectrograph at the Observatoire de Haute-Provence 1.93m telescope, covering the wavelength range 400 to 680 nm. The version of the library employed here corresponds to 1969 spectra of some 1390 stars with a resolving power of R $= 10,000$, publicly available as part of the Elodie.3 release[4] (Moultaka, Ilovaisky, Prugniel, & Soubiran 2004). We smooth the data with a Gaussian kernel to our working resolution. Most spectra have originally a high S/N ratio, which is subsequently enhanced by the smoothing process that we apply. The catalog values of the stellar atmospheric parameters are those included in the FITS headers of the spectra. They come, in most cases, from the literature. The FITS headers also include a quality flag for the atmospheric parameters, and after noticing some outliers with uncertain $T_{\rm eff}$s,

---

[3] http://www.noao.edu/cflib/
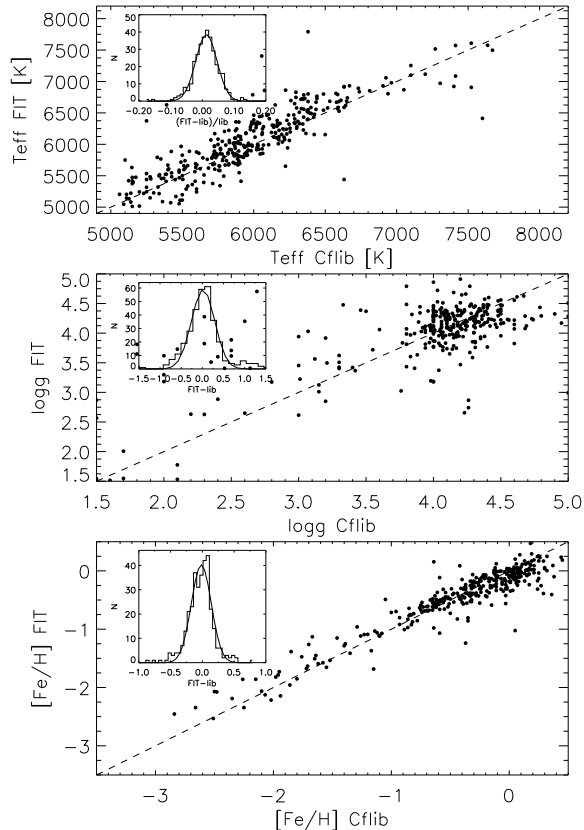[4] http://www.obs.u-bordeaux1.fr/m2a/soubiran/elodie_library.html

FIG. 6.— Comparison between our derived metal abundances (FIT) and those from the catalog of the Indo-US library of Coudé feed stellar spectra (Cflib). The dashed line has a slope of unity. The inset graph shows the abundance differences, and a least-squares fitting to a Gaussian curve.
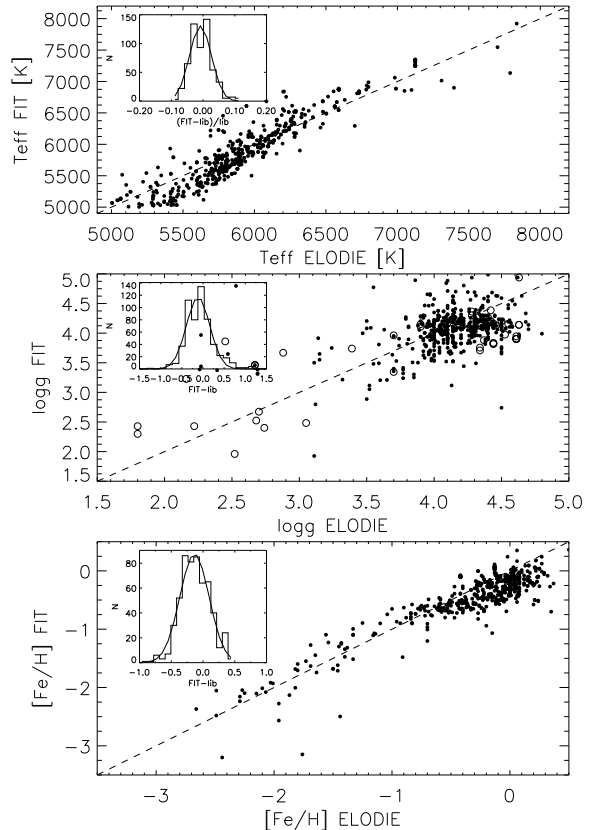
FIG. 7.— Comparison between our derived metal abundances (FIT) and those from the catalog of the ELODIE library. Otherwise similar to Fig. 6.

we decided to limit the comparison to stars with a quality flag in this parameter of at least 1, on the Elodie 0 to 4 scale. The atmospheric parameters for 567 spectra of stars with $5000 < T_{\rm eff} < 8000$ K are compared with our values in Fig. 7. On average, our effective temperatures are lower than Elodie's by 1% ($\sigma = 4\%$), our gravities are lower by 0.12 dex ($\sigma = 0.28$ dex), and our derived abundances are lower by 0.14 dex ($\sigma = 0.23$) dex. The systematic differences in $T_{\rm eff}$ and [Fe/H] are not uniformly distributed, but concentrate on the coolest and more metal-rich stars of the sample. By including cooler stars we are able to sample lower gravities. The open symbols in the middle panel of Fig. 7 correspond to 52 analyzed spectra with derived effective temperatures $4800 < T_{\rm eff} < 5000$ K, and suggest a scatter and systematic offset very similar to those found for warmer stars with higher gravities (filled circles).

After accounting for the systematic differences in $\log g$ and [Fe/H], our derived M_V magnitudes are systematically larger than those listed in the ELODIE catalog. The median difference is 0.52 mag.

3.3. S⁴N

Our third comparison involves the S⁴N survey, which includes spectra for all stars more luminous than $M_V = 6.5$ mag within 14.5 pc from the Sun. These data were

obtained with the 2.7m telescope at McDonald Observatory and the ESO 1.52m telescope at La Silla[5]. This library consists of 118 spectra (for the same number of stars) with wide spectral coverage and a resolving power of R $\simeq 50,000$. Although much more limited in coverage of the atmospheric parameters space than the previous two libraries, this data set is useful because of the very high quality of both the spectra (the S/N ratio is usually larger than 300 at the original resolution) and the catalog of atmospheric parameters. In this sample, there are 77 stars in the range $5000 < T_{\rm eff} < 8000$ K. Fig. 8 shows excellent agreement between the catalog and our estimated atmospheric parameters for these nearby thin-disk stars. The $T_{\rm eff}$ scale of S⁴N is based on the Infrared Flux Method (IRFM; Blackwell & Shallis 1977). The average offset is insignificant, and the 1σ scatter is 2 %, although there is a slight trend with temperature. The gravities, based on *Hipparcos* parallaxes for the S⁴N catalog, are again offset, with our values lower by 0.18 dex, with a scatter of 0.20 dex. The familiar star Capella, with $\log g \sim 2.5$, is the only giant in the sample. The metallicity comparison is again excellent, with our values lower by 0.11 dex, and a scatter of 0.14 dex.

The ultra-precise parallaxes from Hipparcos available for this sample (1 % on average) offer a good opportu-

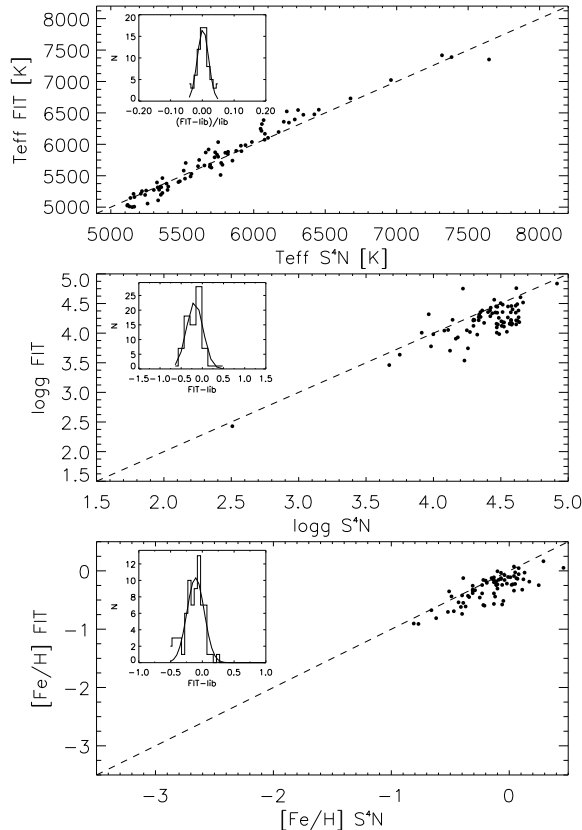[5] http://hebe.as.utexas.edu/s4n/ or http://www.astro.uu.se/~s4n/

FIG. 8.— Comparison between our derived metal abundances (FIT) and those from the catalog of the S^{4}N library. Otherwise similar to Fig. 7.

nity to evaluate the quality of the absolute magnitudes and distances obtained from the comparison with stellar evolution calculations (see §2.2). After correcting our surface gravities for the bias mentioned above, we find that our M_V values are systematically larger than those derived from the Hipparcos parallaxes by 0.5 mag ($\sigma = 0.4$ mag), confirming the offset inferred from the analysis of ELODIE spectra. On average, the derived distances $\log_{10} d = (5 + V - M_V)/5$ are 21 % smaller than the inverse of the parallaxes ($\sigma = 19\%$), with no obvious dependence on the atmospheric parameters.

3.4. The effect of S/N

Our previous comparisons with existing libraries of *nearby* stars helped to established zero points of our scale of atmospheric parameters, as well as to estimate the uncertainties involved in the analysis of real observations. Nonetheless, the spectra included in these libraries have a quality that is far higher than typical SDSS observations. To estimate realistic values for the uncertainties in the derived parameters, we introduce noise in the observations and re-analyze them.

We chose to experiment with spectra from `Cflib`, which are those originally more similar to the SDSS observations. By introducing Poisson noise in the spectra, we degraded them to a S/N per pixel[6] of 160, 80, 40,

---

[6] Our resolution element includes 3 pixels.

20, and 10. We also introduced noise in the $(g - r)$ index, according to the empirical relationship described in §2.2. The results of this experiment are included in Table 1, and suggest that our analysis procedure, and in particular the metallicity determination, is quite robust to reductions in signal-to-noise ratio.

3.5. Empirical corrections

The offsets in surface gravity and metallicity found in the comparison with S^{4}N and ELODIE are very similar, and therefore we conclude that corrections of about +0.15 dex and +0.12 dex should be applied to our gravities and iron abundances, respectively, to match the scale of these libraries. Nevertheless, these libraries are mainly comprised of stars with high metallicities. Closer inspection of the ELODIE analysis shows that the metallicity offset disappears when the comparison is limited to stars with [Fe/H]< -1; this is also supported by the comparison with `Cflib`. Thus, we choose not to correct for this possible offset for the DR3 sample. The offset in surface gravity persists at all metallicities, hence we apply this correction to the values derived in the analysis of DR3 data.

Another important conclusion that emerged from comparison with the ELODIE and S^{4}N samples is that our derived M_Vs appear to be offset by $\simeq 0.5$ mag. This effect may decrease for lower gravities, but because it is clear for dwarfs and subgiants, which make up most of our SDSS sample, we correct for it in our subsequent analysis of DR3 stars. We emphasize that this is equivalent to a correction in the derived distances of about 20 %. As shown below, systematic errors of this order in the stellar distances are inconsequential for our main conclusions.

As can be readily noticed in Figs. 6, 7, and 8, the number of stars with temperatures in the range $7000 < T_{\rm eff} < 8000$ K is very limited. Nevertheless, analysis of the gravities for the ELODIE sample for the few stars in this regime suggests that our surface gravities are overestimated by +0.4 dex, instead of underestimated by ~ 0.12 dex as previously found for the overwhelming majority of stars with cooler temperatures. To avoid poorly understood systematic errors, we restrict the following discussion to the temperature range $5000 < T_{\rm eff} < 7000$ K, approximately equivalent to spectral types F and G.

3.6. Comparisons with other methods on SDSS data

Using Eq. 10 we can easily estimate $B - V$ colors for the DR3 stars analyzed and, by combining this information with the spectroscopically determined surface gravities and metallicities, apply the IRFM calibrations of Alonso et al. (1996, 1999) to estimate effective temperatures. This exercise reveals an intriguing trend, which is illustrated in Fig. 9a. Our derived temperatures (labeled as FIT in the Figure) are systematically higher by an amount that increases with $T_{\rm eff}$. The inset shows the distribution of the differences for two subsets of the sample. For stars with a metallicity [Fe/H] > -1, the mean offset is 162 K ($\sigma = 62$ K), but for [Fe/H] < -1, the average difference increases to 337 K ($\sigma = 109$ K).

Offsets on the order of 100–150 K between the IRFM calibrations and effective temperatures derived from spectroscopy have been repeatedly reported in the literature for disk stars (e.g., Santos, Israelian, & Mayor 2004; Yong et al. 2004; Luck & Heiter 2005; Takeda et
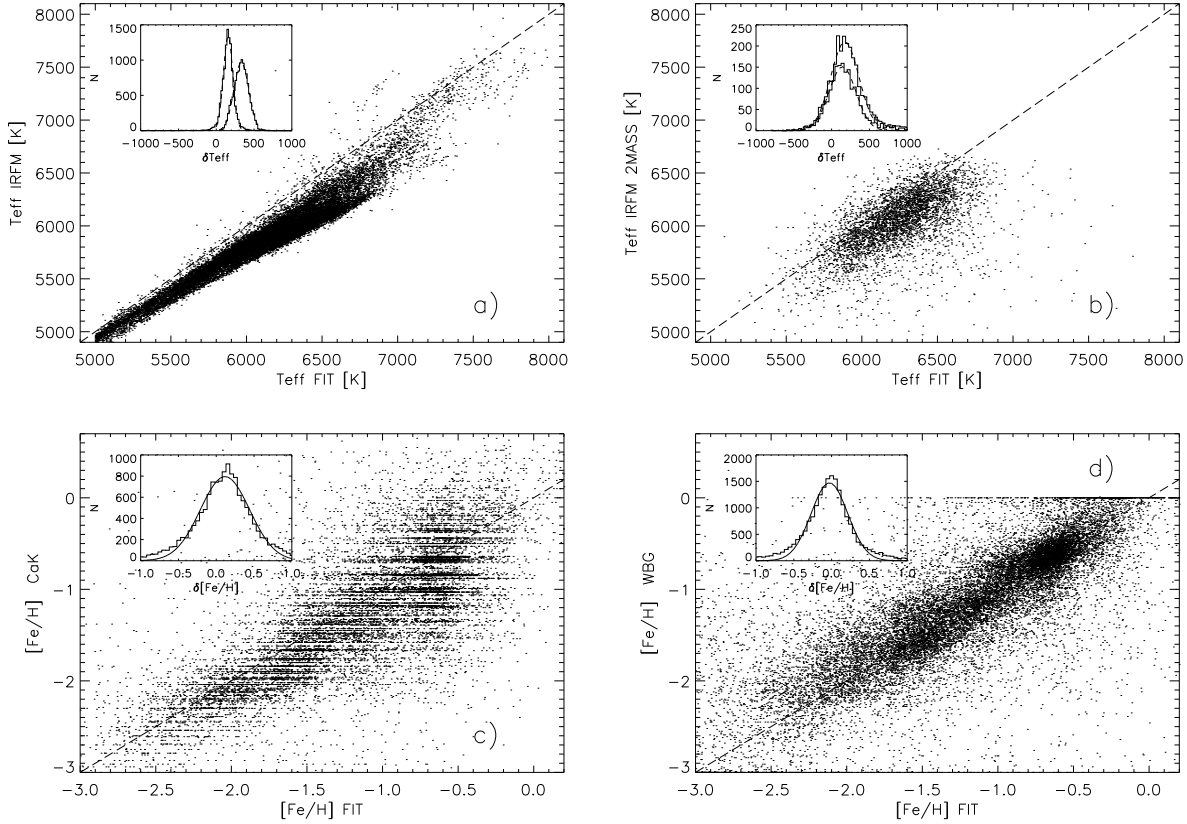
FIG. 9.— a): Comparison between our derived effective temperatures and those from calibrations of optical color indices based on the infrared flux method; b) Similar to a), but for color indices that employ 2MASS observations; c) and d): Comparison between our derived metal abundances (FIT) and those from the 'CaK' and 'WBG' methods (see Beers et al. 1999 and Wilhelm et al. 1999a, respectively). The dashed line has a slope of unity. The inset graphs show the differences (FIT - other; histograms) and a least-squares Gaussian fit, with the sample divided depending on metallicity at [Fe/H]= −1 for panels a) and b).

TABLE 1
OFFSETS BETWEEN OUR DERIVED ATMOSPHERIC PARAMETERS AND THE
CATALOG VALUES

Library	S/N[1]	$T_{\rm eff}$		$\log g$		[Fe/H]	
		$<\Delta>$ (%)	σ (%)	$<\Delta>$ (dex)	σ (dex)	$<\Delta>$ (dex)	σ (dex)
ELODIE	Full	−0.8	3.5	−0.12	0.28	−0.14	0.23
S⁴N	Full	0.2	1.8	−0.18	0.20	−0.11	0.14
Cflib	Full	1.3	3.4	+0.02	0.27	−0.02	0.16
Cflib	160	1.1	3.8	−0.05	0.35	−0.02	0.15
Cflib	80	1.3	3.9	−0.04	0.33	−0.02	0.16
Cflib	40	0.8	3.4	−0.01	0.43	−0.06	0.20
Cflib	20	0.8	4.8	+0.00	0.51	−0.09	0.31
Cflib	10	1.6	8.3	+0.06	0.75	−0.13	0.46

[1]The S/N values here considered correspond to 1 pixel, or 1/3 of a resolution element.

al. 2005). There also exists an indication of a similar effect for F-type stars in the upper panel of Fig. 8. However, the enhanced discrepancies at lower metallicities raise some concern about the use of the $(g − r)$ transformation in Eq. 10 for such stars. We note that our analysis of SDSS data is independent from this transformation, but it plays a role in the comparison with the reference libraries. A transformation that differs somewhat from Eq. 10 has been recently proposed by Bilir,

Karaali,& Tunçel (2005)

$$(g − r) = 1.12431(B − V) − 0.25187, \qquad (11)$$

but our tests revealed that the use of this relation instead of Eq. 10 would only have a very small effect on the comparison with the libraries in the previous sections. Interestingly, the metallicity-dependent discrepancies shown in Fig. 9a would be significantly enhanced by the use of Eq. 11; the same is true if we use instead the transfor-

mations derived for the $u'g'r'i'z'$ system by Smith et al. (2002).

By comparison of our sample with the 2MASS All Sky Catalog (Cutri et al. 2003[7]), we were able to identify 10,210 sources with available 2MASS photometry (JHK_s). The IRFM calibrations recently derived by Ramírez & Meléndez (2005) consider the indices $(V-J)$, $(V-H)$ and $(V-K_s)$, based on 2MASS JHK_s photometry. Unfortunately, applying these calibrations still requires an intermediate step, in order to derive V from g. We can resort to another of the relations derived by Zhao & Newberg:

$$V = g - 0.561(g-r) - 0.004, \qquad (12)$$

or to a combination of Eqs. (1) and (3) of Bilir et al.:

$$V = g - 0.56353(g-r) - 0.03381. \qquad (13)$$

For about 4,000 stars, mostly dwarfs in the range $5500 < T_{\rm eff} < 6500$ K, the IRFM calibrations involving the three 2MASS passbands (ignoring reddening) yield temperatures that agree within 200 K. For those stars, we find a mean systematic offset between our effective temperatures and the IRFM calibrations of 235 K, when Eq. 12 is used, or 173 K when adopting Eq. 13. The distribution of residuals is very similar in both cases, and well approximated by a Gaussian with $\sigma = 180$ K. There is only a minor excursion from the mean offset depending on metallicity (of about 40 K for stars above and below [Fe/H]$= -1$, respectively), as illustrated in Fig. 9b for the case when Eq. 13 is used. Furthermore, the offset is largely independent of $T_{\rm eff}$, and thus approximately equivalent to a correction of ~ -0.1 to the V magnitudes derived from the equations above. Because the Ramírez & Meléndez calibrations are in good correspondence with the temperature scale of the Alonso et al. calibrations, and all our stars are far enough to make distance-dependent extinction corrections implausible, we conclude that the most likely explanation for the systematics in Fig. 9a has to do with the photometric transformations between Johnson and Sloan color indices. Clearly, further work on the derivation of suitable color transformations, especially as a function of metallicity, is required.

We have also compared our iron abundances for stellar spectra in DR3 with the values derived from two different techniques, one based on the equivalent width of the Ca II K and an estimated $B-V$ color ('CaK'; see Beers et al. 1999), and a second based on $ugriz$ photometry and the equivalent width of the Ca II K line, supplemented with spectral synthesis of Balmer lines and molecular bands in the blue region of the spectrum ('WBG'; a refined version of the method described by Wilhelm, Beers & Gray 1999a). The Ca II K line approaches saturation at high metallicity and cooler temperatures, but it should be a reliable indicator at low metallicity. Fig. 9c confronts the two scales for 18,727 DR3 stars with $(B-V) < 1$, or spectral types earlier than K0. On average, our iron abundances are higher than those obtained from the CaK method by 0.12 dex, with a 1σ scatter of 0.33 dex, which is reduced for stars with [Fe/H]< -1. Over much of the range of [Fe/H], the comparison with the WBG values

for 20,990 stars shows less scatter than with the CaK method, only 0.24 dex, and no detectable offset, as illustrated in Fig. 9d. However, the scatter in the estimated [Fe/H] is lower when compared with the CaK approach at the lowest metallicities.

Our derived distances can be compared with those obtained purely from photometry, using the main-sequence relationship (Bilir et al. 2005)

$$M_g = 5.791(g-r) + 1.242(r-i) + 1.412. \qquad (14)$$

On average, the distances based on the spectroscopic parameters are 0.33 dex (or 76 %) smaller than the photometric version, with a 1σ scatter of about 20 %. The comparison in §3.3 showed that our inferred distances were biased by only ~ 20 %, and therefore we believe most of the discrepancy with the photometric distances is likely related to issues with the latter.

3.7. *Duplicates*

DR3 includes some instances of multiple observations of the same stars in different plugplates. Among the 44,175 DR3 spectra for which we successfully identified Balmer lines, there are 1,022 duplicates, 11 objects with three spectra, and 1 star with 4 observations. For these cases, the S/N ratio of the spectra were very similar, given the uniform exposure times used in SDSS, and thus we retained the averaged values for the stellar parameters. The parameters derived from multiple spectra of the same object are remarkably consistent The mean rms scatter (basically the average difference, for most of the multiple observations are just duplicates) in $T_{\rm eff}$, $\log g$, and [Fe/H] are 16 K, 0.09 dex, and 0.07 dex, respectively.

4. RESULTS FROM DR3

Fig. 10 shows the projected positions of the selected SDSS stars on the sky (equatorial coordinates α,δ) on the galactic plane (polar coordinates R, ϕ), where

$$R = \sqrt{(R_\odot - d\cos b\cos l)^2 + (d\cos b\sin l)^2}, \qquad (15)$$

$$\sin\phi = -\frac{d\cos b\sin l}{R}, \quad \text{and}$$

$$\cos\phi = \frac{R_\odot - d\cos b\cos l}{R}, \qquad (16)$$

and in cartesian galactic coordinates ($x = R\cos\phi$, $y = R\sin\phi$, $z = d\sin b$). The solar position in the top left-hand panel is at $\phi = 0$ and $R_\odot$, the galactocentric distance of the Sun, which is taken as 8 kpc. The gaps in coverage on the galactic plane result from those of the DR3 footprint on the sky.

The selection effects involved in choosing SDSS spectroscopic targets are complex, and we have imposed additional cuts in effective temperature. Our final sample includes 22,770 F- and G-type stars with $5000 < T_{\rm eff} < 7000$ K and $S/N > 30$; their distribution in the g vs. $(g-r)$ plane is shown in Fig. 11a. Some patches in the density of stars are obvious, such as the 16 stars per plate targeted, in similar proportions, as flux calibrators ($g < 17$, $0. < g - r < 0.6$) or reddening *standards* ($g < 18.5$, $0 < g - r < 0.6$). These standards are

---

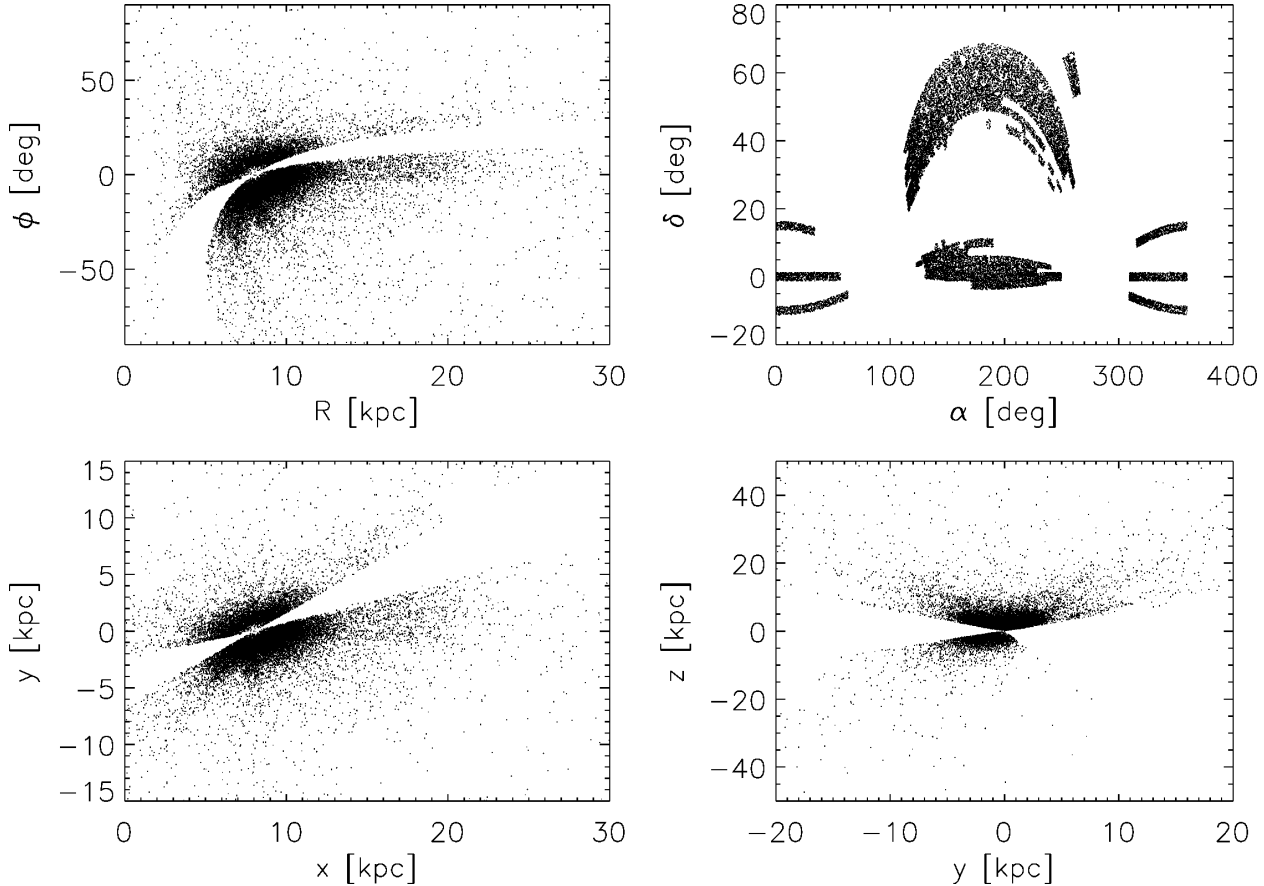[7] http://www.ipac.caltech.edu/2mass/index.html

FIG. 10.— Projected positions of the DR3 stars selected for analysis on the galactic plane (top left-hand panel), on the sky (top right), and on galactic cartesian coordinates (bottom panels).

also subjected to two more color cuts $0.6 < u - g < 1.2$ and $g - r > 0.75(u - g) - 0.45$, which introduce a bias against high-metallicity ($[Fe/H] > -0.5$) stars. In addition, standard-star candidates are prioritized based on the proximity of their colors to those of the SDSS standard halo subgiant BD +17 4708, which strengthens the bias. The density of stars at the red end is artificially enhanced in DR3, as brown-dwarf candidates were given a high priority, but they have been excluded from Figure 11 for being outside the domain that our analysis can handle. A similar bias applies to A-type horizontal-branch candidates with $(g - r) < 0.2$. The distribution of DR3 spectroscopic targets resembles the distribution of photometric point sources for $16.5 < g < 18.5$ and $0.5 < (g - r) < 0.85$, but unfortunately the distance range covered by the brightest dwarfs in that range is limited to $1 < d < 3$ kpc, which is insufficient to properly map the falloff of the stellar density of the thick disk.

4.1. Metallicity distribution

Fig. 11b shows the number of stars as a function of distance from the galactic plane, $z = d \sin b$, assuming the Sun is at $z = 0$. The combination of two exponential laws provides a reasonable approximation for the star counts. Even though we cannot properly derive the stellar density of the Galaxy from the star counts, we can certainly associate, based on previous work, the majority of the stars within $1 < |z| < 3$ kpc with the thick-

disk population and virtually all of those at $|z| > 8$ kpc with the halo population. More specifically, assuming scale heights $Z_{thin}^h \simeq 0.25$ kpc and $Z_{thick}^h \simeq 0.8$ kpc, and a normalization factor $\rho_{thick}/\rho_{thin} \sim 0.1$, more than 83 % of the stars at $1 < |z| < 3$ kpc are members of the thick disk; this number would be enhanced if metal abundances are considered. Adopting a spherical halo whose density falls from the galactic center as a power-law with an exponent of -2.44 (Robin et al. 2003), and a ratio $\rho_{thick}/\rho_{halo} \sim 40$ at the solar position, we find that more than 99 % of the stars at $|z| > 8$ kpc are members of the halo.

The sample considered here contains 12,483 stars at $1 < |z| < 3$ kpc and 2,838 at $|z| > 8$ kpc. Figure 12a shows the metallicities and distances from the plane for individual F-type stars ($6000 < T_{eff} < 7000$ K). Histograms of the metallicities of the stars in these two $|z|$ ranges are shown in Fig. 12b (solid: $1 < |z| < 3$ kpc; dashed: $|z| > 8$ kpc). Figs. 12c and d are the equivalent diagrams for G-type stars ($5000 < T_{eff} < 6000$ K). No significant differences are found between the metallicity distribution function of stars in the North or South galactic hemispheres.

Some of the most metal-rich stars in the sample at $|z| < 1$ kpc are most likely members of the thin-disk population. As was previously found for EDR spectra, dwarfs and subgiants with SDSS spectra in DR3 trace the thick disk (with some contamination from the thin
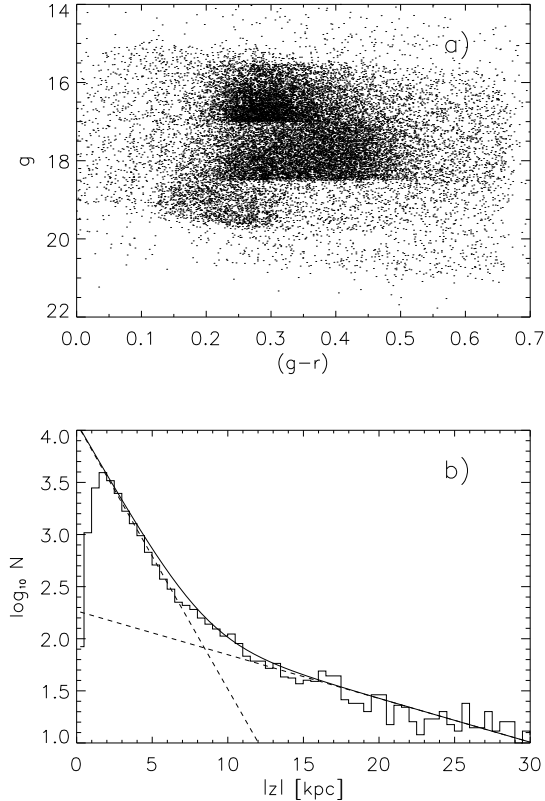
FIG. 11.— *a*): Distribution of the stars selected for analysis on the $g-(g-r)$ plane. The large numbers of F-type subdwarfs selected as flux calibrators are obvious in the range $0.2 < (g-r) < 0.5, 15.5 < g < 18.5$. *b*): Number of stars in the sample as a function of distance from the galactic plane. The stars counts are reasonably well-fit with a combination of two exponential laws (dashed lines).

disk), while the brighter and more evolved stars belong mostly to the halo (Allende Prieto et al. 2004b). The halo metallicity distribution, as derived from the stars at $|z| > 8$ kpc, peaks approximately at [Fe/H] ~ -1.4, and contains stars with a wide range of metallicities. The peak of the metallicity distribution function of the thick disk (metal-rich peaks at $1 < |z| < 3$ kpc) is located at about [Fe/H] $\simeq -0.7$, in good agreement with previous determinations (e.g., Gilmore, Wyse, & Jones 1995). The distribution of F-type stars close to the plane shows a second-peak roughly at the same metallicity of the distant halo stars. We expect that some of these stars belong to the metal-weak thick disk, (see Beers et al. 2002 and references therein), but most do not share the kinematics of the more metal-rich thick-disk stars (see §4.3).

The frequency of spectroscopic binaries with periods shorter than 10 yr among nearby (thin-disk) field stars is about 14 % (Halbwachs et al. 2003). Those with a mass ratio $q < 0.5$ are most likely to be mistaken as single stars in our analysis with no consequences, but those with $q > 0.8$, which may represent as many as half of all binaries, have the potential to distort somewhat our results. Twin systems of F- or G-type stars will be confused by our procedures with single objects with lower effective temperatures (by 100-200 K) and lower metallicities (by ~ 1 dex); albeit the Hβ profile would be poorly matched.

Because our metallicity distribution for F-type stars is composed of similar numbers of stars at [Fe/H] $= -1.5$ and $= -0.7$, this bias is unlikely to be significant. The contamination could be larger for G-type dwarfs, and deserves more detailed consideration in the future.

The thick-disk metallicity distribution seems to end abruptly at about solar metallicity, but this result is affected by the bias against high-metallicity stars imposed by the color selection of the SDSS spectrophotometric and reddening standards. The contribution of thin-disk stars close to the plane to the solid line in Fig. 12d, is negligible, as the shape of the distribution remains essentially undisturbed when $|z|$ is restricted to the range $2 < |z| < 3$ kpc. Again, changes are hardly noticeable if we extend the range to $0 < |z| < 3$ kpc. Most of the low-metallicity G-type stars near the plane exhibit halo kinematics (see §4.3). Close examination of the G-type dwarfs with metallicities [Fe/H] > -1.2 within the range $1 < |z| < 3$ kpc reveals a mean metallicity [Fe/H] $= -0.685 \pm 0.004$, a median value of [Fe/H] $= -0.679$, and a 1σ dispersion of 0.238 dex. No vertical metallicity gradient is apparent in this well-sampled region of the thick disk. If such a gradient is present, it must be smaller than 0.03 dex kpc^{-1}.

The metallicity peak associated with F-type halo stars is slightly shifted to higher metallicities at larger distances from the plane (See Fig. 12b). Because of the selection effects involved, this shift cannot be interpreted as a metallicity gradient in the halo. Thick-disk stars at $|z| < 3$ kpc might shift the peak of the halo metallicity distribution to slightly higher values, and so potentially induce a metallicity shift in the opposite sense to what is observed. On the other hand, constant magnitude limits might easily cause a metallicity bias in the sense that we observe. The absolute magnitude of a mid-F dwarf is about $M_g = 4$ at solar metallicity, and 1 mag fainter at [Fe/H]$= -1.7$. For the limits of the SDSS standards previously discussed, namely $15.5 < g < 18.5$, we are biased against high-metallicity F dwarfs at distances $d < 4$ kpc and against low-metallicity objects at $d > 5$ kpc.

An enhancement is apparent in the metallicity distribution of distant F-type stars at [Fe/H] ~ -2.9. No spatial or kinematic coherence is apparent for these stars. Phenomenological models of galaxy formation in the framework of cold dark matter predict a similar feature in connection with the abrupt end of the infall phase (Qian & Wasserburg 2004). For halos originated from 2σ density fluctuations the interpretation of the peak at this low metallicity would be that infall cessation took place almost simultaneously with the start of astration, about 0.5 Gyr after the Big Bang. Because of the uncertainties involved due to small number statistics, more data are necessary to confirm the reality of this feature in the metallicity distribution.

Fig. 13 shows the variations of stellar metallicities as a function of the galactocentric distance projected onto the plane, R (see Eq. 15). The solid lines track the median metallicity in 1 kpc bins for stars at $|z| > 8$ kpc, and for those with $5000 < T_{\rm eff} < 6000$ K at $1 < |z| < 3$. Halo stars ($|z| > 8$ kpc) exhibit a metallicity distribution that is essentially independent of galactocentric distance. The thick-disk population, identified with the G-type stars closer to the plane, can only be traced up to $\sim \pm 4$kpc from $R_\odot$. These stars also exhibit a flat or very small
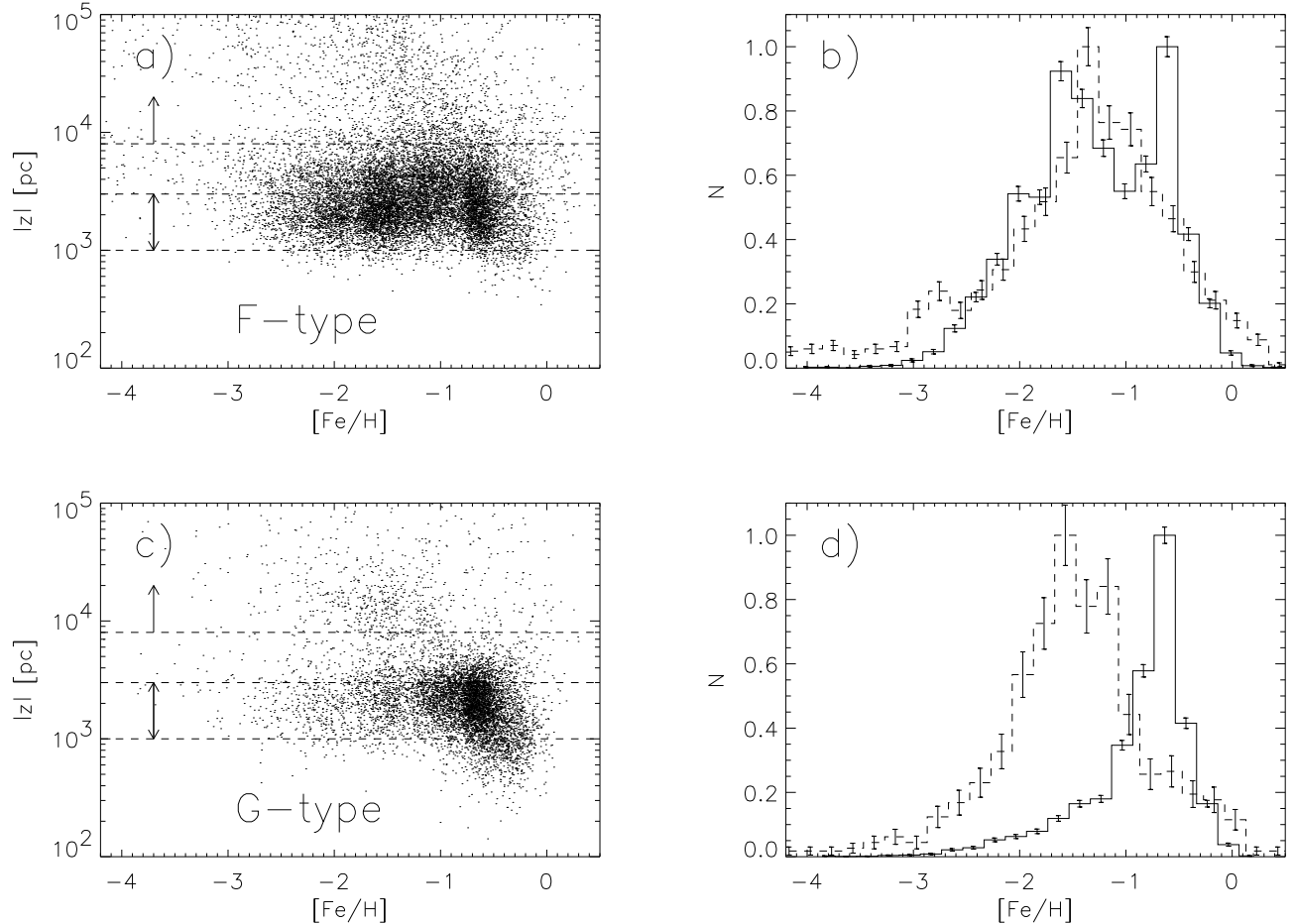
FIG. 12.— *a)* Metallicity distribution of the F-type stars in the sample (6000< T_{eff} < 7000 K) as a function of distance from the galactic plane; *b)* The stars in panel a) between 1 and 3 kpc from the plane (solid) and those farther away than 8 kpc (dashed line) are binned in 0.2 dex intervals to calculate the histograms shown. There are 7,422 stars at |z| < 3 kpc and 2,107 stars at |z| > 8 kpc; *c) and d)* Similar to a) and b), but only including G-type stars (5000< T_{eff} < 6000 K). There are 5,061 stars at |z| < 3 kpc and 731 stars at |z| > 8 kpc.

metallicity variation, in contrast with the marked gradient found in the thin disk from open clusters, Cepheids, H II regions, or massive stars (e.g., Twarog, Ashman, & Anthony-Twarog 1997; Andrievsky et al. 2004; Vílchez & Esteban 1996). The dashed line in Fig. 13 illustrates the average metallicity gradient in thin-disk OB-type stars derived by Daflon & Cunha (2004) over the range in galactocentric distance spanned by their study.

We note that the metallicity gradient of the thin disk may disappear beyond $R \sim 10 - 12$ kpc (Twarog et al. 1997; Yong et al. 2005), and in that regime the observed abundance ratios show a more complicated behavior than what is observed in the solar neighborhood (Yong et al. 2005). By comparing radial abundance gradients measured from planetary nebulae, open clusters, cepheids, H II regions, and OB stars and associations, Maciel, Lago & Costa (2005) conclude that the thin-disk gradient is now more flat by a factor of 2–3 compared with its value 8 Gyr ago – when star formation in the thick disk may have ended.

Our analysis suggests that in the temperature range $5000 < T_{\text{eff}} < 7000$ K, our sample contains over 150 stars with [Fe/H]< −3, and over 2000 stars with [Fe/H]< −2.

A few stars with [Fe/H] < −4 may be present in this sample, but additional data are required to confirm their extreme metallicities.

4.2. Ages

The changes between the metallicity distributions for $1 < |z| < 3$ kpc in panels b (F-type stars) and d (G-type stars) of Figure 12 indicate that in this range of |z| there are both halo and thick-disk populations present among the F-type stars, but thick-disk members dominate the sample of G-type stars. The SDSS targets metal-poor F-type stars for calibration purposes, but in this range of |z|, thick-disk stars should overwhelm the halo population, as it is apparent among G-type stars. The presence of large numbers of halo F-type dwarfs close to the disk is not the result of halo stars being younger than the thick-disk population. It is instead a natural reflection of the fact that metal-poor stars, despite living slightly shorter lives, have significantly warmer surface temperatures. For any given age, the main-sequence turn-off is located at higher T_{eff}s at [Fe/H]=−1.4 than at [Fe/H]=−0.7. The bias against high-metallicity stars induced by the color-based selection of the SDSS stellar
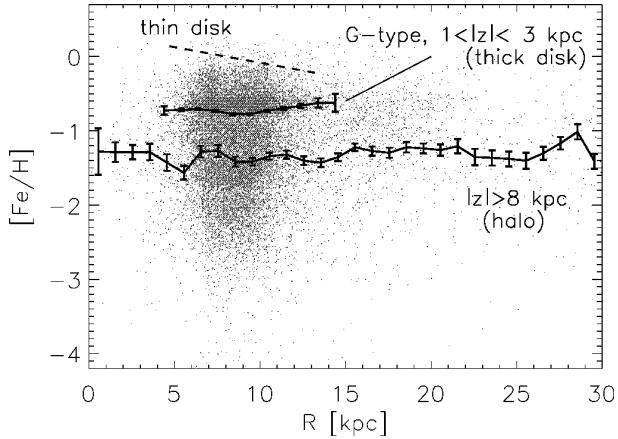
FIG. 13.— Metallicity distribution of the stars in the sample as a function of galactocentric distance on the plane. All of the stars with $5000 < T_{eff} < 7000$ K are shown with gray dots. The solid lines correspond to the median values in 1 kpc bins for stars more than 8 kpc from the galactic plane (here tentatively identified as members of the halo), and to those with $5000 < T_{eff} < 6000$ K located between 1 and 3 kpc from the plane (a sample presumably dominated by thick-disk stars).
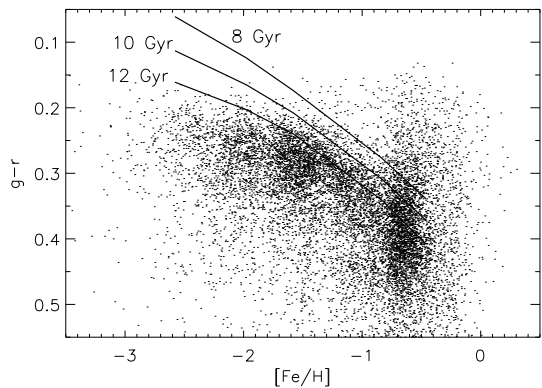

FIG. 14.— The color index $g - r$ (corrected for reddening) and metallicities for F- and G-type dwarfs and subgiants ($\log g > 4$) in the range $1 < |z| < 4$. The solid lines trace the position of the main-sequence turnoff as a function of metallicity for ages 8, 10, and 12 Gyr.

targets is more severe at redder colors (i.e., our G-types), and therefore must be a minor contributor. We can be more quantitative below, with the caveat that absolute ages are more difficult to estimate than relative numbers, and are subject to larger systematic errors.

Fig. 14 shows the $(g-r)^8$ index as a function of the derived metallicity for the stars in the range $1 < |z| < 3$ kpc for which we derived a high value of the gravity $\log g > 4$. The imposed distance selection automatically removes giants, and our gravity selection ensures such an exclusion. Similar diagrams have been previously discussed by Gilmore, Wyse & Kuijken (1989). The turnoff stars define an upper envelope in this diagram, which traces the oldest populations at any given metallicity. Using isochrones from Girardi et al. (2004), we have determined the loci of the turnoff as a function of metallicity

---

[8] As always in this paper, we refer to photometry corrected for reddening (see §2.1).

for different ages, accounting for the enhanced $[\alpha/Fe]$ ratios using Eq. 9. We note that the predicted surface temperatures for turnoff stars in the Yonsei-Yale isochrones (Yi, Kim & Demarque 2003) are very similar to those used here. The stars with $[Fe/H] < -1$ suggest that star formation in the halo ceased between 10 and 12 Gyr ago.

In general, very old ages, usually > 10 Gyr, have been reported for thick-disk stars (see, e.g., Carney, Latham, & Laird 1989; Quillen & Garnett 2001; Reddy et al. 2003, 2005). Fig. 14 does not contradict those findings, but strongly supports that some members of the thick-disk are at least as young as 8 Gyr.

4.3. Kinematics

Additional insight on the nature of the stellar populations in the DR3 spectroscopic sample may be obtained by exploiting the information provided by radial velocities. An issue of particular interest is the rotation speed of the different galactic components. Assuming any given star is simply moving in a circular orbit around the Galaxy with a velocity V_{rot} in a cylindrical coordinate system with its origin at the center of the Galaxy (R, ϕ, z), we have $\mathbf{V} = -V_{rot}\mathbf{u}_\phi$, where $\mathbf{u}_\phi$ is the unit vector in the azimuthal direction. Further assuming that the Sun is on a circular orbit in the galactic plane, with a velocity $\mathbf{V}_\odot = -V_\odot\mathbf{u}_\phi$, V_{rot} can be inferred from the star's position and the measured heliocentric radial velocity, V_r:

$$V_{rot} = \frac{V_\odot R \sin\phi - V_r d}{R_\odot \sin\phi}$$

$$= \frac{R}{R_\odot} \left(V_\odot + \frac{V_r}{\cos b \sin l} \right). \quad (17)$$

We avoid the approximation that the Sun is in a circular orbit by replacing, in Eq. 17, $V_\odot$ by the velocity of the local standard of rest (LSR; adopted as 220 km s^{-1}, Kerr & Lynden-Bell 1986), and V_r by the radial velocity with respect to the LSR

$$V'_r = V_r + U_\odot \cos b \cos l + V_\odot \cos b \sin l + W_\odot \sin b, \quad (18)$$

where the solar peculiar motion relative to the LSR is $(U_\odot, V_\odot, W_\odot) = (10.1, 4.0, 6.7)$ (Hogg et al. 2005).

Fig. 15 shows the derived V_{rot} as a function of the distance to the plane for our sample. This transformation is appropriate only for stars that have a purely azimuthal velocity. Therefore, it is a good approximation only for thin-disk stars, as reflected by the small intrinsic scatter close to the galactic plane. However, the median V_{rot} values for any given population should be robust, and therefore statistically meaningful (for reasonable values of b), as far as the Milky Way is approximately axisymmetric. Fig. 15 shows the median rotation velocity derived for all stars, and two subgroups, in 0.1 dex bins. (Error bars are standard errors for a mean value assuming a Normal distribution). This exercise reveals a smooth variation of the median rotation velocities. The nearest stars approach the thin-disk rotation, while, as the distance from the plane increases, the inferred rotation velocity decreases up to a distance of 4 kpc. A vertical asymmetry is clearly present in the region where most of the stars concentrate, between 1 and 3 kpc ($3 < \log_{10}|z| \lesssim 3.5$). The lower solid line shows the median values for stars
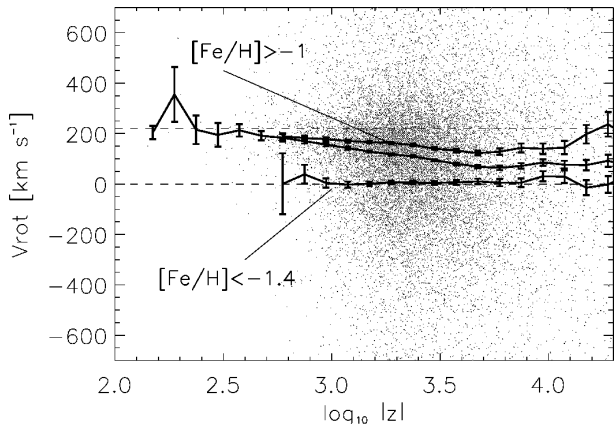
FIG. 15.— Rotational velocity for individual stars derived assuming solid-rigid rotation as a function of the stars' distance to the galactic plane. The lines show the median value in non-overlapping 0.1 dex bins for all stars, and two subgroups separated by metallicity. The dashed lines mark the canonical values for the LSR (220 km s^{-1}) and no rotation.
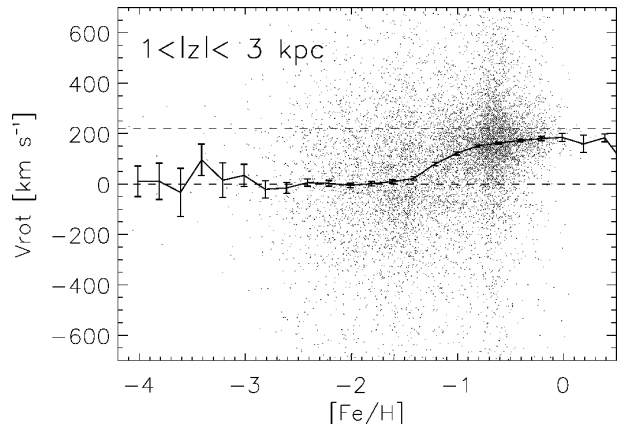

FIG. 16.— Rotational velocity for individual stars at $|z| < 3$ kpc derived assuming solid-body rotation. The solid line shows the median value in non-overlapping 0.2 dex bins in metallicity. The dashed lines mark the canonical values for the Sun (220 km s^{-1}) and no rotation.

with a metallicity [Fe/H]< −1.4, and confirms that the galactic halo exhibits essentially no rotation. The upper line corresponds to stars with [Fe/H]> −1; it should be dominated by the thick-disk population at $1 < |z| < 3$ kpc, but is contaminated by halo stars at larger distances from the plane.

Based on the same model described in §4.1, up to 18 % of our sample in the range $1 < |z| < 3$ would be part of the stellar halo, while none of the stars would belong to the halo with a more restrictive window between $1 < |z| < 2.4$ kpc. These figures are based on star counts alone. Selecting only the stars with [Fe/H]> −1 should practically remove all halo stars in the range $1 < |z| < 3$ kpc. When this is done, a vertical gradient in the derived median rotational velocity for thick-disk stars is apparent: $V_{rot} = 192(\pm 8) - 0.016(\pm 0.004)|z|$ km s^{-1}. This gradient was determined using all F- and G-type stars, but we obtain a result that is statistically indistinguishable when only G-type stars are used (ensuring a more complete removal of halo stars). Our analysis, thus, lends support to previous measurements of a gradient by Majewski (1992), who derived −21 km s^{-1} kpc $^{-1}$, and the reanalysis of his data by Chen (1997; −14±5 km s^{-1} kpc $^{-1}$), although we derive a flatter slope that the determination by Chiba & Beers (2000), who found −30 ± 3 km s^{-1} kpc $^{-1}$.

A more detailed dissection of the dependence of the estimated galactic rotation velocities on metallicity close to the plane ($1 < |z| < 3$ kpc) is shown in Fig. 16. The solid line joins again the median values for the different bins. This line remains essentially unchanged if the graph is restricted to G-type stars. Thick-disk stars, here identified as moderately metal-poor objects, lag the thin disk rotation by 0–100 km s^{-1}, with a median value of 157±4 km s^{-1} at [Fe/H]=−0.7. In Fig. 16, the stars with −3 < [Fe/H] < −1.4 exhibit a flat rotation profile; the majority of these objects are most likely halo members, with very limited contamination from possible members of the metal-weak thick-disk population. The average value for stars located at $|z| > 8$ kpc with metallicities [Fe/H]< −1.4 is $V_{rot} = −25 ± 15$ km s^{-1}, a result that

appears independent from the distance to the plane, as the median values in Fig. 15 suggest.

5. DISCUSSION AND SUMMARY

We have analyzed a large number of stellar spectra included in the SDSS third data release (DR3). By extensive comparison with modern spectroscopic libraries and catalogs of atmospheric parameters, we have shown that our analysis procedure is capable of deriving effective temperatures, surface gravities, and iron abundances with a 1σ accuracy of 3 %, 0.3 − 0.4 dex, and 0.2 dex, respectively, based on SDSS photometry and spectroscopy. We estimate a relative precision of 20 % in the inferred distances to dwarfs and subgiants, with systematic errors of similar size.

As a result of the selection of bright $0.2 < (g−r) < 0.4$ stars to calibrate SDSS spectra, significant numbers of F-type subdwarfs are included in the DR3 spectroscopic sample. Many moderately metal-poor (−1 <[Fe/H]< −0.4) late-F and early G-type dwarfs and subgiants are also present in the sample. We associate the observed distributions of distant metal-poor stars that show small galactic rotation velocities with the halo population, and the closer $V_{rot} \sim 160$ km s^{-1} G-type stars of intermediate metallicity with the thick disk, with the caveat that selection effects may make the observed distributions in space and velocity significantly different from the true volume-limited distributions.

The halo population shows a broad distribution of iron abundances which peaks at about [Fe/H] = −1.4, while the thick-disk stars exhibit a much narrower distribution with a sharp maximum near [Fe/H] = −0.7. Halo stars follow a metallicity distribution that appears independent of galactocentric distance on the plane; the same is true for the thick-disk population between 5 and 14 kpc, in contrast with the marked gradient typically found in the thin disk. No vertical metallicity gradient is discernible in the thick disk between $1 < |z| < 3$ kpc. A clear vertical gradient is, however, detected in the thick-disk asymmetric drift. A linear least-squares fit to the median galactic rotational velocities of putative thick-disk dwarfs between 1 and 3 kpc from the plane indicates a slope of −16 km s^{-1} kpc^{-1} and, if the linear trend is

extrapolated, a maximum rotation speed of 192 km s^{-1} (or a lag of 28 km s^{-1} from the LSR) at $z = 0$.

F-type stars at distances from the plane $|z| < 3$ kpc exhibit galactic rotation velocities that are much lower than for thick-disk stars with higher metallicities, and are consistent with the majority of them being drawn from the halo population. The presence of these stars is naturally explained due to their lower metallicity compared to the thick-disk population, which results in warmer surface temperatures for a given mass. The halo population appears to be older than about 11 Gyr, while there are thick-disk stars which are at least 2 Gyr younger.

Models for the formation of the thick disk must satisfy several constraints now apparent in the observations: (1) metal abundance ratios that are distinct from those of thin-disk stars, (2) the lack of metallicity gradients both in the radial and the vertical directions, (3) a vertical gradient in the rotation velocity, and (4) the existence of thick-disk stars that are about 8 Gyr old, and thus overlap in age with the oldest stars in the thin disk. Hierarchical merging in the context of cold dark matter has been recently shown to be compatible with the enhanced α/Fe ratios and the lack of metallicity gradients (Brook et al. 2004, 2005), but it remains to be seen whether it is consistent with the observed vertical variation of rotational velocity. Gilmore, Wyse & Norris (2002) argue that this is possible, as the debris from the merging satellites will end up in higher, more slowly-rotating orbits than stars newly formed due to the heating of the thin disk, but detailed simulations are necessary.

Efforts to acquire and study more complete and substantially less-biased samples with the (SDSS) ARC 2.5M telescope and spectrographs are underway. The Sloan Extension for Galactic Understanding and Exploration (SEGUE) aims at expanding SDSS imaging coverage, in particular at lower galactic latitudes, over the next three years of operation. A substantial fraction of the 250,000 stars selected for medium-resolution spectroscopy as part of SEGUE will be a homogeneous sample of G-type dwarfs; their space densities, abundances, and kinematics will set substantially tighter constraints on models of the structure and evolution of the Milky Way.

REFERENCES

Abazajian, K., et al. 2004, AJ, 128, 502

Abazajian, K., et al. 2005, AJ, 129, 1755

Adelman-McCarthy et al. 2005, ApJS, in press (astro-ph/0507711)

Allende Prieto, C. 2004, AN, 325, 604

Allende Prieto, C., Barklem, P. S., Lambert, D. L., & Cunha, K. 2004a, A&A, 420, 183

Allende Prieto, C., Beers, T. C., Li, Y., Newberg, H. J., Wilhelm, R., & Yanny, B. 2004b, Carnegie Observatories Astrophysics Series, Vol. 4: Origin and Evolution of the Elements, ed. A. McWilliam and M. Rauch (Pasadena: Carnegie Observatories, http://www.ociw.edu/ociw/symposia/series/)

Alongi, M., Bertelli, G., Bressan, A., Chiosi, C., Fagotto, F., Greggio, L., & Nasi, E. 1993, A&A, 97, 851

Alonso, A., Arribas, S., & Martínez-Roger, C. 1996, A&A, 313, 873

Alonso, A., Arribas, S., & Martínez-Roger, C. 1999, A&AS, 140, 261

Andrievsky, S. M., Luck, R. E., Martin, P., & Lépine, J. R. D. 2004, A&A, 413, 159

Asplund, M. 2005, ARA&A, in press

Asplund, M., Grevesse, N., & Sauval, A. J., to appear in Cosmic Abundances as Records of Stellar Evolution and Nucleosynthesis, ASP Conf. Ser., 2005, F.N. Bash and T.G. Barnes, eds., in press

Bensby, T., Feltzing, S., & Lundström, I. 2003, A&A, 410, 527

Beers, T. C. 1999, Galaxy Evolution: Connecting the Distant Universe with the Local Fossil Record, Proceedings of the Rencontres de l'Observatoire - 1998, M. Spite, ed., Kluwer Academic Publishers, p. 105

Beers, T. C., Drilling, J. S., Rossi, S., Chiba, M., Rhee, J., Führmeister, B., Norris, J. E., & von Hippel, T. 2002, AJ, 124, 931

Beers, T.C., Preston, G.W., & Shectman, S.A. 1992, AJ, 103, 1987

Beers, T. C., Rossi, S., Norris, J. E., Ryan, S. G., & Shefler, T. 1999, AJ, 117, 981

Bertelli, G., Bressan, A., Chiosi, C., Fagotto, F., & Nasi, E. 1994, A&A, 106, 275

Bilir, S., Karaali, S., & Tunçel, S. 2005, AN, 326, 321

Blackwell, D. E., & Shallis, M. J. 1977, MNRAS, 180, 177

Bressan, A., Fagotto, F., Bertelli, G., & Chiosi, C. 1993, A&A, 100, 647

Brewer, M.-M., & Carney, B. W. 2005, AJ, in press (ArXiv Astrophysics e-prints, arXiv:astro-ph/0509267)

Brook, C. B., Gibson, B. K., Martel, H., & Kawata, D. 2005, ApJ, 630, 298

Brook, C. B., Kawata, D., Gibson, B. K., & Freeman, K. C. 2004, ApJ, 612, 894

Brown, W. R., Allende Prieto, C., Beers, T. C., Wilhelm, R., Geller, M. J., Kenyon, S. J., & Kurtz, M. J. 2003, AJ, 126, 1362

Brown, W. R., Geller, M. J., Kenyon, S. J., & Kurtz, M. J. 2005, ApJ, 622, L33

Cabrera-Lavers, A., Garzón, F., & Hammersley, P. L. 2005, A&A, 433, 173

Carney, B. W., Latham, D. W., & Laird, J. B. 1989, AJ, 97, 423

Chen, B. 1997, AJ, 113, 311

Chen, B., et al. 2001, ApJ, 553, 184

Chiba, M., & Beers, T.C. 2000, AJ, 119, 2843

Chiba, M., & Beers, T.C. 2001, ApJ, 549, 325

Christlieb, N. 2003, Reviews of Modern Astronomy, Vol. 16, 191

Cutri, R. M., et al. 2003, VizieR Online Data Catalog, 2246. Originally published in: University of Massachusetts and Infrared Processing and Analysis Center, IPAC/California Institute of Technology

Daflon, S., & Cunha, K. 2004, ApJ, 617, 1115

Degl'Innocenti, S., Prada Moroni, P. G., & Ricci, B. 2005, ArXiv Astrophysics e-prints, arXiv:astro-ph/0504611

Edlén, B. 1966, Metrologia, Vol. 2, No. 2, 71

Fagotto, F., Bressan, A., Bertelli, G., & Chiosi, C. 1994, A&A, 104, 365

Freeman, K., & Bland-Hawthorn, J. 2002, ARA&A, 40, 487

Fuhrmann, K. 1998, A&A, 338, 161

Fuhrmann, K., Pfeiffer, M., Frank, C., Reetz, J., & Gehren, T. 1997, A&A, 323, 909

Gilmore, G., Wyse, R. F. G., & Jones, J. B. 1995, AJ, 109, 1095

Gilmore, G., Wyse, R. F. G., & Kuijken, K. 1989, ARA&A, 27, 555

Girardi, L., Grebel, E. K., Odenkirchen, M., & Chiosi, C. 2004, A&A, 422, 205

Halbwachs, J. L., Mayor, M., Udry, S., & Arenou, F. 2003, A&A, 397, 159

Hill, G. J. & MacQueen, P. J. 2002, Proc. SPIE, 4836, 306

Hogg, D. W., Blanton, M. R., Roweis, S. T., & Johnston, K. V. 2005, ApJ, 629, 268

Hubeny, I. 1988, Comp. Phys. Comm., 52, 103

Hubeny, I., Hummer, D. G., & Lanz, T. 1994, A&A, 282, 151

Hubeny, I., & Lanz T. 2000, Synspec: – A User's Guide, available from http://tlusty.gsfc.nasa.gov

Kerr, F. J., & Lynden-Bell, D. 1986, MNRAS, 221, 1023

Kurucz, R. L. 1993, ATLAS9 Stellar Atmosphere Programs and 2 km/s grid. Kurucz CD-ROM No. 13, Cambridge, Mass.: SAO

Larsen, J. A. & Humphreys, R. M. 2003, AJ, 125, 1958

Lenz, D. D., Newberg, J., Rosner, R., Richards, G. T., & Stoughton, C. 1998, ApJS, 119, 121

Luck, R. E., & Heiter, U. 2005, AJ, 129, 1063

Maciel, W. J., Lago, L. G., & Costa, R. D. D. 2005, A&A, 433, 127

Majewski, S. R. 1992, ApJS, 78, 87

Moore, A. M., Gillingham, P. R., & Saunders, W. 2002, Proc. SPIE, 4836, 299

Moultaka, J., Ilovaisky, S. A., Prugniel, P., & Soubiran, C. 2004, PASP, 116, 693

Nelder, J., & Mead, R. 1965, Computer Journal, 7, 308

Newman, P. R., et al. 2004, Proc. SPIE, 5492, 533

Nordström, B., Mayor, M., Andersen, J., Holmberg, J., Pont, F., Jorgensen, B.R., Olsen, E.H., Udry, S., & Mowlavi, N. 2004, A&A, 418, 989

Norris, J. E. 1999, Ap&SS, 265, 213

Prochaska, J. X., Naumov, S. O., Carney, B. W., McWilliam, A., & Wolfe, A. M. 2000, AJ, 120, 2513

Prugniel, P., & Soubiran, C. 2001, A&A, 369, 1048

Qian, Y.-Z., & Wasserburg, G. J. 2004, ApJ, 612, 615

Quillen, A. C. & Garnett, D. R. 2001, ASP Conf. Ser. 230: Galaxy Disks and Disk Galaxies, 87

Ramírez, I., & Meléndez, J. 2004, A&A, 417, 301

Reddy, B. E., Tomkin, J., Lambert, D. L., & Allende Prieto, C. 2003, MNRAS, 340, 304

Reddy, B. E., Lambert, D. L., & Allende Prieto, C. 2005, MNRAS, submitted

Robin, A. C., Reylé, C., Derrière, S., & Picaud, S. 2003, A&A, 409, 523

Santos, N. C., Israelian, G., & Mayor, M. 2004, A&A, 415, 1153

Schlegel, D. J., Finkbeiner, D. P., & Davis, M. 1998, ApJ, 500, 525

Siegel, M. H., Majewski, S. R., Reid, I. N., & Thompson, I. B. 2002, ApJ, 578, 151

Smith, J. A., et al. 2002, AJ, 123, 2121

Soubiran, C., Bienaymé, O., & Siebert, A. 2003, A&A, 398, 141

Stoughton, C., et al. 2002, AJ, 123, 485

Strauss, M., & Gunn, J. E. 2001, Technical Note available from http://archive.stsci.edu/sdss/documents/response.dat

Strauss, M. A., et al. 2002, AJ, 124, 1810

Takeda, Y., Ohkubo, M., Sato, B., Kambe, E., & Sadakane, K. 2005, PASJ, 57, 27

Twarog, B. A., Ashman, K. M., & Anthony-Twarog, B. J. 1997, AJ, 114, 2556

Valdes, F., Gupta, R., Rose, J. A., Singh, H. P., & Bell, D. J. 2004, ApJS, 152, 251

Vílchez, J. M., & Esteban, C. 1996, MNRAS, 280, 720

Wilhelm, R., Beers, T. C., & Gray, R. O. 1999a, AJ, 117, 2308

Wilhelm, R., Beers, T. C., Sommer-Larsen, J., Pier, J., Layden, A. C., Flynn, C., Rossi, S., & Christensen, P. R. 1999b, AJ, 117, 2329

Yi, S. K., Kim, Y.-C., & Demarque, P. 2003, ApJS, 144, 259

Yong, D., Lambert, D. L., Allende Prieto, C., & Paulson, D. B. 2004, ApJ, 603, 697

York, D. G., et al. 2000, AJ, 120, 1579